BAR ILAN AND YESHIVA UNIVERSITIES

RESEARCH SYMPOSIUM

AUGUST 6TH AND 7TH 2013

The BIU-YU Summer Science Research Internship program places select undergraduates in one of the state-of-the-art research laboratories of Bar-Ilan's Life Science, Exact Science, or Engineering Faculties. It enables talented undergraduate science majors to take part in the research of one of Bar-Ilan's more than 180 distinguished science and engineering faculty members.

Av & Em Bayit:
Rav Eliav and Adi

A Collection of Research Abstracts from the BIU-YU Summer Science Research Internship 2013

Program Director
Prof. Chaim Sukenik

Tradition of Excellence

Bar-Ilan University

TABLE OF CONTENTS

CHEMISTRY

COMPUTER SCIENCE / MATHEMATICS / PHYSICS

ENGINEERING

LIFE SCIENCES

NEUROSCIENCE / PSYCHOLOGY

Edited, compiled and designed by Aaron Javitt, Meir Moshe Kurtz and Shaina Sedighim

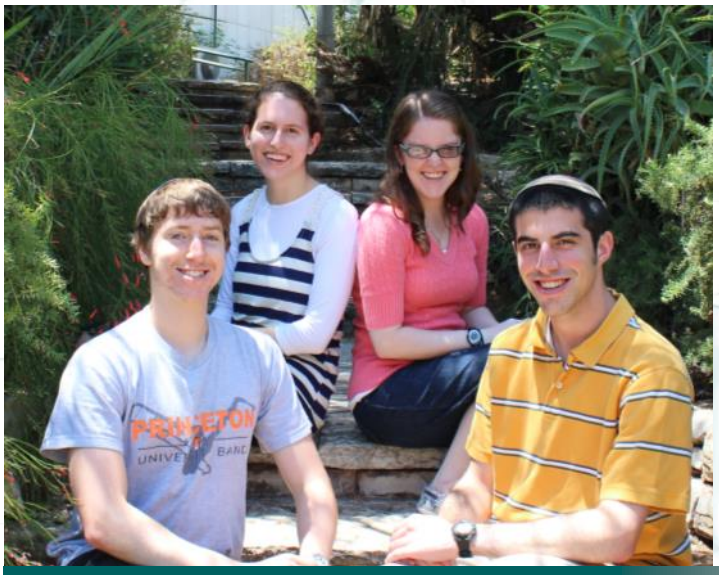

From left to right: Gideon Grossman , Gabriela Dobkin, Zeeva Levine , Yaakov Tuchman

MEDICINAL CHEMISTRY :: FISCHER LAB

Gabriela Dobkin (Stern College, Biochemistry) "The development of NPP1 inhibitors for the treatment of Osteoarthritis/CPPD disease."

Osteoarthritis (OA) and Calcium Pyrophosphate Dihydrate (CPPD) deposition disease are joint pathologies. Symptoms of OA and CPPD include: pain, stiffness, and loss of joints function. The onset of osteoarthritis often begins at the age of 40-50. By the age of 80 it affects most people to various degrees. However, OA and CPPD may also occur in young people upon an injury or as a result of an operation performed on a joint. These diseases currently have no cure and pose a serious threat to the quality of the sufferer's life. Several recent studies have established a relationship between chrondocalcinosis (CPPD crystal deposition at the joints) and the pathogenesis of osteoarthritis. CPPD crystals, which are often detected in the synovial fluid, cause stiffness and severe pain and may eventually lead to cartilage damage. CPPD crystals are produced from calcium ions and extracellular pyrophosphate. The latter is produced from ATP hydrolysis by ecto-nucleotidase NPP1. Hence, NPP1 inhibitors were suggested as potential therapeutic agents for the treatment of CPPD and OA. To date, this hypothesis has not been tested.

This project involved the synthesis of non-hydrolyzable nucleotide analogues which can eventually be employed as extracellular NPP1 inhibitors. Specifically, this project worked on synthesizing ATP-α-CH_2-γ-S which has already shown promising in vitro results when tested on the NPP1 enzyme (showing a Ki of 20 nm and an IC50 of 0.39 μm). The final product of the multi-stage synthesis will be further tested on the Chondrocyte cells and the matrix vesicle. Quantification of the effect of inhibitors on chondrocytes' NPP1 mediated ATP hydrolysis, as a function of the expression level of NPP1 will then be tested.

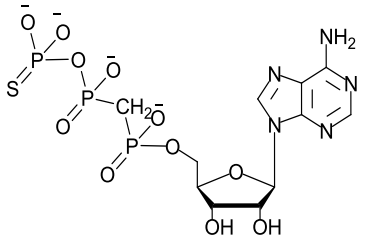

Figure 1: ATP-α-CH_2-γ-S

In addition, this project works on synthesizing a potential NPP1 inhibitor that has yet to be tested on the enzyme 2-SMe-ADP(α-S). The inhibitor is being investigated in hopes of being used as a more stable alternative to the previously mentioned analogue. Upon completion, this compound will be tested in similar ways as ATP-α-CH_2-γ-S was tested in order to determine its stability and efficiency as an inhibitor of NPP1.

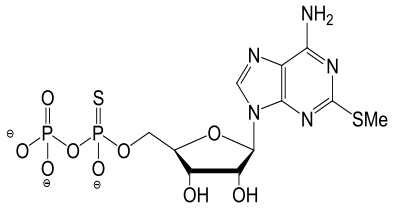

Figure 2: 2-SMe-ADP(α- S)

Throughout the multi-stage synthesis, purification techniques were used to separate our product from the by-products. Such techniques include: liquid chromatography (LC), reverse phase high

pressure liquid chromatography (HPLC) (both preparatively and analytically) and column chromatography. In these synthesis precautions were taken to ensure that the reactions remained free of water. This was done by performing most reactions under nitrogen gas as well as freeze-drying the products to evaporate the water that was present. In addition, Nuclear Magnetic Resonance (NMR) was used after the various steps of the reaction to verify that product reception.

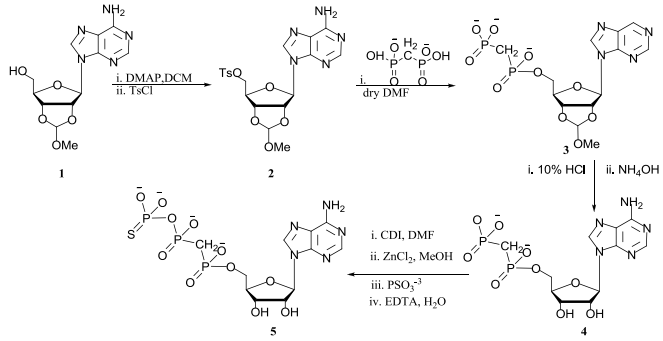

Figure 3: The synthesis of ATP-α-CH_2-γ-S

CHEMISTRY —NANOTECHNOLOGY :: ZABAN LAB

Gideon Grossman (Princeton University, Mechanical Engineering) "KrF pulsed laser deposition of Cr_xO_y and W_xO_y thin films and their potential to serve as absorber layers in all-oxide thin film solar cells"

Solar photovoltaic energy has decreased in price and increased in efficiency from 1% in 1883 to around 29% today[1]. Yet, the cost of all existing technologies, from conventional silicon-based solar cells[2] to newer GaAs, CIGS, and dye-sensitized cells, is still greater than the cost of electricity from fossil fuels. Moreover, many of these structures are toxic, degrade quickly, and require high-energy fabrication. In the hopes of overcoming these obstacles, Professor Arie Zaban's lab in Bar Ilan University is researching a new type of solar cell made of metal-oxide thin films[3]. This new structure may convert solar energy into electricity with a higher efficiency, lower cost, and longer lifespan than conventional solar cells. Thin films are chemical layers with thicknesses on the order of Angstroms to a few micrometers[4]. All-oxide thin film solar cells consist of several layers of metal oxide thin films. Metal oxides are attractive materials because they are thermodynamically stable, nontoxic, naturally abundant, and easy to fabricate.

The central goal of this experiment was to find an effective material for the absorber layer. This is where most of the photon absorption takes place in a thin film solar cell. Six samples were fabricated using KrF excimer laser ablation (PLD) in a combinatorial approach[5]. Cr_xO_y and W_xO_y were deposited under varied parameters, namely temperature, pressure, laser fluence and repetition rate, substrate material and target to substrate distance, that affect film outcome. O_2 was the ambient gas for every deposition. The subscripts "x" and "y" in "Cr_xO_y" and "W_xO_y" indicate either undetermined or non-uniform atomic ratios[6]. Chromium and tungsten oxides were chosen because they have not been thoroughly studied as solar cell candidates and have interesting technological applications. For instance, smart windows benefit from tungsten's electrochromic properties and liquid crystal displays contain Cr_2O_3. The desired phase in the chromium oxide depositions was Cr_2O_3, because it is the most thermodynamically stable chromium oxide phase.

First, the metal oxides were only deposited as independent layers in order to find a material with good adhesion and semi-transparency[7]. Adhesion was observed with an Olympus AX70 microscope. The libraries were tested for phase and crystal structure with X-ray diffraction (XRD). The Cr_xO_y deposited on FTO at 400°C and 5.5x10^-4 Torr showed good adhesion and semitransparency. Over the next week, this library's optical properties, including abrsorptance and bandgap, will be determined with an optical scanner. The deposition was repeated as a layer within a complete solar cell so that an I-V scanner will be able to measure the library's photovoltaic properties, including V_{oc}, I_{sc}, h and FF. The solar cell was fabricated on glass coated with FTO (the front contact) and an n-type window layer of TiO_2. Ag back contacts were deposited with RF sputtering and tin was soldered around the edges. At best, this material will prove to be an effective p-type absorber. If not, the data obtained in this experiment will be a useful addition to the thin film material database and will help guide the direction of future experiments.

---

1. 29% does not include the higher efficiencies (up to 44%) of tandem (stacked) cells, which are very expensive and only used for niche purposes.

2. A solar panel is a collection of solar cells that are wired together.

3. The Zaban lab is also researching dye sensitized and quantum dot solar cells.

4. 1 angstrom = 10^-10. Thin films have many applications including two-way mirrors, antireflective coatings, toxic gas sensors, low-emissivity windows that help maintain a comfortable temperature inside homes year round, drug delivery, and batteries. Some existing thin film solar cells are flexible, allowing panels to be installed in novel applications, such as rooftop shingles and tents. Currently, the all-oxide thin films fabricated in the Zaban lab are deposited on hard substrates because the immediate priority is energy conversion performance. In the future, however, it may be possible to fabricate flexible all-oxide thin films.

[5] In the combinatorial approach, samples are fabricated with gradients of properties, such as thickness and phase. The ability to fit a large amount of information on one sample, appropriately called a "library", accelerates the search for useful materials. Material property results from each experiment are stored in a growing computer database. A program compares points from many libraries to find correlations and trends that in turn guide material selection for future experiments. The database is also useful for applications other than solar energy.

[6] When raw material assembles on the substrate, it often changes phase. The film's identity must be characterized by methods such as X-ray diffraction (XRD) and Raman spectroscopy.

[7] Greater transparency indicates higher oxygen content and therefore a more stable phase. Semi-transparency is desired because the solar cell should absorb visible light – the portion of the electromagnetic spectrum in which solar radiation is most intense.

CHEMISTRY —NANOTECHNOLOGY :: ZABAN LAB

Yaakov Tuchman (Yeshiva College, Physics) "Perovskite sensitized photovoltaic cells."*

Solar radiation presents a highly promising source of renewable energy. Photovoltaic devices have gone through several generations, from first generation cells based on a semiconductor p-n junction, through the cheaper, albeit less efficient second generation devices developed in previous decades. Recently, much research has been invested in third generation devices, intended to be both efficient and relatively cheap.

With the introduction of dye-sensitized solar cells (DSSC) in 1991, a new era of photovoltaic devices began. The operating principle of these cells was to assign each of the various stages of photoconversion to a separate material, which would allow for individual optimization of each step. DSSC, and subsequently in 2008, quantum dot sensitized solar cells (QDSSC), used a thin mesoporous layer of oxide as a nanostructure upon which the sensitizer could be deposited. The oxide layer would conduct the electrons away from the sensitizer, while a conductive redox electrolyte would transport the holes to the cathode, thus generating a photovoltage.

Recent developments in the field of perovskite sensitized solar cells have indicated the potential for further research, with record-breaking photoconversion efficiencies reported as reaching 15%. The most common perovskite used is the organic-inorganic metal halide perovskite, $CH_3NH_3PbI_3$. The perovskite mineral structure allows for more streamlined cells, incorporating the hole conducting layer into the photon absorber. However, among the factors that can negatively affect the perovskite layer is the presence of moisture which can cause the perovskite to oxidize, greatly lowering both the cell's stability and overall performance. Because of the heightened sensitivity to moisture, as much of the process as possible is restricted to a glove-box in which moisture levels are maintained at only a few ppm.

As this is a new field for this laboratory, much of our research has been devoted to high-order optimizations, attempting to synthesize cells of comparable quality to those published. Although the cells synthesized physically exhibit signs of successful deposition of the perovskite mineral, results have yet to match those of the reported values. In attempt to understand these results, further research was done on nearly every level of the cells.

In the past few years, it has been shown that the thickness of the mesoporous layer can greatly affect the efficiency of sensitized solar cells. For this research, mesoporous layers of Titanium Dioxide were deposited via various methods, particularly the doctor-blade method for layers between 4 and 10 microns, spin-coating with restricted boundaries for layers around 1 micron, and screen printing for layers between 400 and 1000 nanometers.

Various solvents were used in the synthesis of the perovskite, as well as multiple deposition methods. In the deposition of the perovskite, we followed two methods: spin-coating of the complete precursor solution, and the sequential deposition method presented by Professor Michael Grätzel in a recent publication. Based on this research, we verified that the crystal structure of the deposited perovskite matches the published structures.

In the deposition of the metal back contact, both silver evaporation and gold sputtering were used, with better performance resulting from the evaporation. Research has already been conducted on the effect that the work functions of various metals can have on the overall efficiency. Consequently, these results may be taken as an indication of the physical damage that the sputtering process could do to the delicate perovskite layer.

While further research is needed, this work provides a basis for further development of the synthesis of perovskite sensitized solar cells.

*Under the guidance of Ronen Gottesman and Dr. Shay Tirosh.

CHEMISTRY

COMPUTATIONAL CHEMISTRY :: MAJOR LAB

Zeeva Levine (Stern College, Mathematics) "Visualization of hydrogen wavefunctions in chemical and biological systems"

Enzymes are efficient catalysts, performing well-defined and highly specific chemical reactions. High-accuracy computation of the rates of enzymatic reactions must include nuclear quantum mechanical effects (NQE), because quantum mechanical effects such as tunneling and zero-point energy play an important role in such reactions. In particular, the behavior of lightweight nuclei such as hydrogen in condensed phases is strongly affected by NQE.

There are multiple methods for performing quantum mechanical calculations on a system. In her PhD work, Hamutal Engel of Professor Dan Major's lab used the less-conventional Feynman path integral (PI) simulation method in which the quantum density matrix is written as a PI. She used this method because PI formulations can be used in mixed quantum-classical systems where certain atoms are quantized while others are treated classically and because Feynman PI's in particular are easily extended to multidimensional systems.

Hamutal and Professor Major developed an efficient numerical method called the Path Integral Eigenvalue method (PI-EV), which is based on Feynman PI formulations of the density matrix and computes NQE in chemical and biological systems, allowing for accurate calculation of chemical reaction rates. PI-EV, which can be applied to low- or high- dimensionality systems, uses an efficient eigenvalue computation of the thermal density matrix and yields eigenvalues (energy levels) and eigenfunctions (wavefunctions) from which many quantum physical and chemical properties of the system can be determined. The method was first applied to simple model systems, then to chemical systems which are significantly impacted by NQE, and eventually to several prototype enzymes whose process involves the transfer of a hydride ion.

My role was then to analyze the wavefunctions visually inside the chemical and biological systems. I created a Fortran code that converts the output file of eigenfunctions, which appears as a long list of numbers, into a Gaussian Cube file. This file can be read by molecular modeling programs such as Visual Molecular Dynamics (VMD) and displayed along with the actual molecule on which the calculations were performed.

Visualization of results is a crucial step in the process of obtaining qualitative and quantitative insights into the quantum nature of chemical and biological processes. The conversion of raw data into a familiar image allows information to be gleaned that would be difficult to obtain otherwise; many phenomena that are easily seen by eye are virtually impossible to obtain from looking at a long list of numbers.

One molecule to which the PI-EV and then my code were applied is tropolone. Tropolone ($C_7H_6O_2$) is a planar, conjugated, nearly-symmetric, seven-carbon ring with oxy- and hydroxyl- substitutions at the 1 and 2 positions. Its tautomerization includes an O-HO → OH-O transfer, and spectroscopic experiments have determined that this shift involves proton tunneling. Thus tropolone can be used as a model system for the investigation of H tunneling in enzymatic reactions.

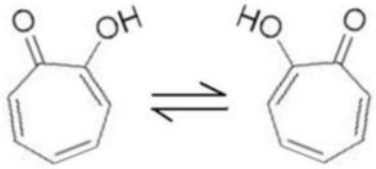

Figure 1. *Tropolone tautomerization*

After the wavefunctions, related to the probability of finding the atom of interest in a particular spot and showing its movement, were calculated and converted into a Gaussian Cube file, the data was read into VMD 1.8.6 with a model of tropolone.

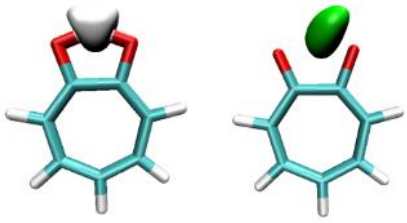

a b

Figure 2. *Isosurface reresentation of the ground state vibrational wavefunctions in tropolone (a) Reactant state, (b) Transition state*

This visualization does, in fact, give some interesting information that would otherwise be difficult to know; the reactant state wavefunction is not completely symmetric – it bulges more at the bottom, closer to the second oxygen. This demonstrates an increased probability of finding the hydrogen atom closer to the second oxygen, due to an attraction between the two atoms. The transition state wavefunction, on the other hand, is absolutely symmetric because the system itself is symmetric, and it is delocalized between the two oxygens.

Just as application of PI-EV and my code on tropolone yielded important information, the same can be done for more complicated chemical and biological systems.

Engel, Hamutal (2013) Discretized Path Integral Methods & Nuclear Quantum Effects in Multi-Dimensional Systems.

COMPUTER SCIENCE / MATHEMATICS / PHYSICS

From left to right: Gabriella Elkaim, Caleb Leibowitz, Yair Hillman, Joshua Lockerman, Adam Ariel, Aryeh Stiefel, Ayelet Friedman

MATHEMATICS :: COHEN LAB

Adam Ariel (Yeshiva College, Mathematics) "Percolation of overlaid random graphs"

Erdős–Rényi random graphs achieve percolation for a given probability of edge connection as a function of the number of nodes. By taking two random graphs overlaid on the same set of vertices, we can find, using computer simulation, a first-order phase transition from joint-small- to joint-giant-components in the graph. We attempted to find an analytic solution to this transition. Using an inclusion-exclusion probability-based inequality, we worked to find analytic upper and lower bounds on the point of transition by considering forced bifurcation of larger and larger collections of vertices as a test for being a giant component. By taking a limit of the above function we searched for a formulation of the percolation point in terms of the number of nodes. The goal is to establish upper and lower bounds which are similar to the computer simulated results. The full range of our bounds is yet to be determined.

PHYSICS :: KALISKY LAB

Gabriella Elkaim (Stern College, Physics) "Scanning SQUID microscopy"

Lanthanum Aluminate (LAO) and Strontium Titanate (STO) are both non-magnetic, insulating, complex oxide materials. Yet, when layered, the interface between them can exhibit electrical and magnetic properties including conductivity, superconductivity and ferromagnetism on the nanoscale. We use superconducting quantum interference devices (SQUIDs) to probe the properties of LAO/STO interfaces. Knowledge of the magnetic properties of these surfaces is useful due to their small size and low dimensions which makes them good candidates for nanotechnological applications. The small size and quantity of their physical properties is also why we need extremely sensitive techniques to detect them. For example, the interface magnetism appears as tiny ferromagnetic islands that cannot be detected with conventional scientific tools.

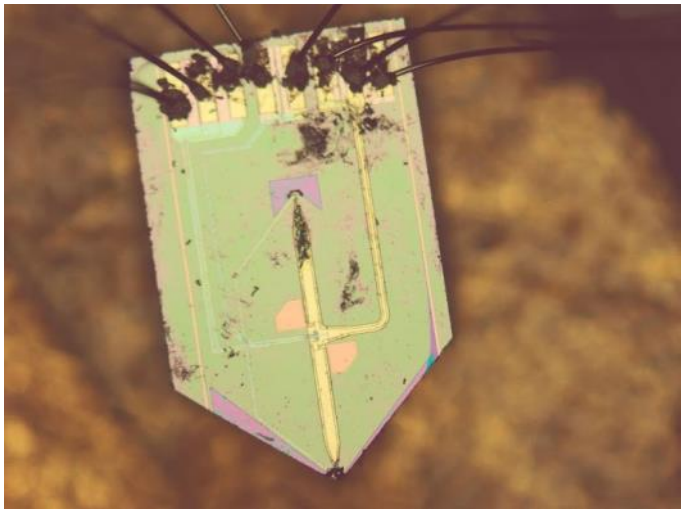

SQUIDs are used to measure a sample's natural magnetic field as well as its susceptibility. It is based on the behavior of superconductors at junctions with non-superconducting material. It has a complex fabricated structure to accommodate its electronics and to reach the goal of making space sensitive measurements of small scale samples. Each SQUID is less than a millimeter wide and

includes two Josephson junctions, modulation coils, field coils and pickup loops. For the purpose of magnetometry, the SQUID is placed over a sample and the magnetic field of the sample threads the loop and changes its critical current with periodicity of the basic flux quantum, Φ_0. For the purpose of susceptometry, a current is passed through the field coil inducing a local magnetic field in the sample. The response of the sample is then detected by the pickup loop, as in magnetometry.

As part of the building of the scanning squid microscope system, the summer was spent testing and measuring the SQUIDs, which are the heart of the system, and planning the circuitry that will be necessary for collecting data during measurement. I worked with Bat-el Dahan, a graduate student in Dr. Kalisky's lab, to take microscopic images of 38 squids. I also measured and documented the resistance of the different parts of the SQUIDs at room temperature using a probe station with two needles connected to a Keithley measuring device. Finally, we were able to measure two of the SQUIDs at temperatures where it superconducts. We placed the SQUIDs in a physical property measurement system (PPMS) and cooled them to about 2 Kelvin. Both measured SQUIDs were found to be malfunctioning. During the process we found a way remove the protective polymer covering the SQUIDs from only the measuring pads, and not the SQUID circuitry. This enables us to keep the SQUID protected during the cool down and electrical tests.

I was able to accomplish this by using my eyelashes to clean the pads with acetone.

Since the SQUID is such a sensitive device it is important not to pass too high a current through it, lest the SQUID be damaged. Still, in order to collect data we need to be able to raise and lower the amount of current passing through the SQUID. In order to do this without harming the SQUID I used a 20 KΩ potentiometer in conjunction with two resistors of 1 KΩ and 59 KΩ to design a circuit whose current can be adjusted from 0-400 μA when attached to a 24 V voltage source. In addition to this, we had to design a low pass electronic filter in order to reduce noise in our measurements once the scanner is built. After learning how to weld from Dvir Hadad, an undergraduate assistant to Dr. Kalisky, I designed and built a filter consisting of two 5.36 KΩ resistors and a 1 μF capacitor, so that its cutoff frequency is 30 Hz.

Using these apparatuses we will be able to use the SQUIDs I prepared to probe LAO/STO interfaces.

MATHEMATICS :: DR. REUVEN COHEN

Ayelet Friedman (Stern College, Mathematics) "Improving the convergence rate and information accuracy for autonomous robots executing the algorithms 'spread' and 'fast-spread'"

Autonomous robots are indistinguishable, lack means of communication, operate in discrete cycles, can be oblivious (have no memory) or non-oblivious, and can use local (know only positions of neighboring robots) or global (know positions of all robots) algorithms. The systems can be modeled as synchronous (all robots move in each time cycle) or asynchronous.

The specific problem I looked at was a fully synchronous, oblivious, local system of robots in a one-dimensional configuration in which we want the robots to spread out equidistant from each other. The algorithm "Spread" in Dr. Cohen's paper suggests that each robot compute its new position based on the previous position of the robots around it. If $R_i[t]$ is the position of robot i at time t, then the algorithm tells the robot to moves to

$$R_i[t+1] = \frac{R_{i+1}[t] + R_{i-1}[t]}{2}.$$

Using the Discrete Fourier Sine Transform, we find that this algorithm will cause the robots to converge to the desired spread and the progress term which tracks the shift from the desired location will at least be halved every $\frac{\ln 2}{2c}N^2$ steps, where c is a constant and N is the number of robots.

In an attempt to improve the convergence rate of the robots, a new equation was suggested:

$$R_i[t+1] = \frac{R_i[t]}{2} + \frac{R_{i+1}[t] + R_{i-1}[t]}{4}.$$

My calculations concluded that this would improve the rate of convergence but only by a constant factor, not by orders of magnitude as desired.

For the same equidistant spread in a non-oblivious, global (robots know they are number i out of n) system we have an algorithm called "Fast-Spread." Using the information obtained from the knowledge of successive positions of neighboring robots, the robot can calculate the position of its nth neighbor at time 0. In order for all the robots to obtain all the information they would need in order to calculate their final positions, N-2 steps would be needed. The information accuracy decays quickly because the coefficients of the terms are proportional to 2^{-n+k-1} where n is half the total number of robots and k is the robot's position from the

nearest end.

In order to account for this accuracy error we try to allow the robots to obtain the information about the boundary robots more directly by responding to the n-th neighbor's position in the n-th step. So, in the first step, the robot executes the algorithm based on the first neighbors. In the second step, having obtained information from the first neighbors about the second neighbors, the robot can execute the algorithm based on the positions of the second neighbors in the initial position. Each of the robots can continue to calculate in this way until all the information reaches the robots on the ends and then each of the robots can move into position based on their knowledge of the positions of the end robots and their index in the lineup. In this way there can be less dilution as the information propagates across the system.

PHYSICS :: GARINI LAB

Yair Hillman (Yeshiva College, Physics) "DNA's dancing duo: chromatin telomere relative diffusion dynamics"

This project addresses the relative dynamics between telomeres and chromatin in the nucleus. In order to measure their relative motion, the telomeres and chromatin of U20S and MEF cells were tagged with fluorescent proteins. The telomere was stained with TRF1-RFP (Red fluorescent protein), and the chromatin was stained with H2B-PAGFP (a histone with photo activatible green fluorescent protein). A small region of the chromatin was activated with precise wavelength laser targeting.

The advantage of using photo-activatable fluorescent tagging for chromatin is that it allows one to distinguish a small area of the chromatin in the nucleus and track the motion of a telomere relative to the activated chromatin. Using confocal fluorescent microscopy, real time videos of the moving telomeres and chromatin were produced. In order to analyze the motion, a program was designed. The program determines the intensity center of mass of each the telomere and chromatin structures. Using these centers of mass, trajectories were extracted and the relative MSD (mean square displacement) between the telomere and chromatin was calculated. Next, we built a simulator in order to determine the accuracy of our program and find the optimal threshold for disregarding error from noise (1.3*median intensity). Our results showed that: A) the tagging was accurate, because the histone-less telomere showed significantly reduced green fluorescence (Fig. 1). B) Based on our analysis of the relative MSDs, it seems that the telomere follows normal diffusion relative to the surrounding chromatin (Fig 2). This preliminary experiment only included 8 cells and had a simplified model of study. Future issues that need to be addressed include: analysis of the 3rd dimension of telomere-chromatin motion and the chromatins' internal structural shifting.

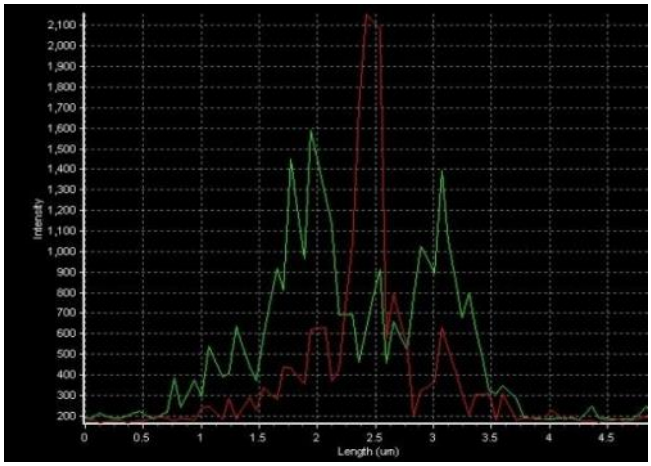

Fig. 1— An intensity diagram. The green line indicates activated tags on the chromatin histones, and the red line indicates the RFP bound to the telomere. Note that there is a significant drop in the expression of green fluorescence near the telomere, due to the fact the telomere is not packed around histones.

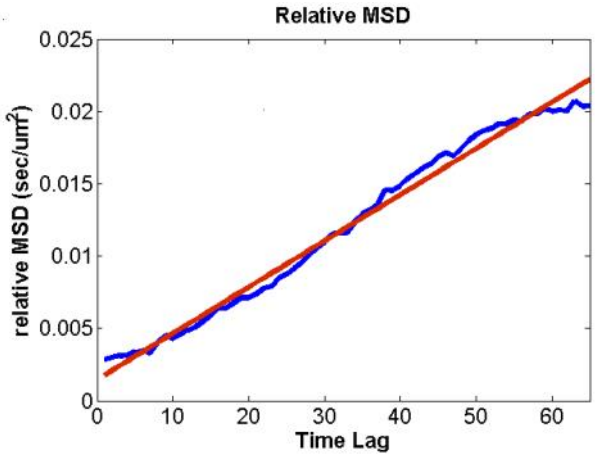

Fig 2.—A graph of the relative MSD for one of the cells. This graph shows the essentially linear graph of the telomere- chromatin relative MSD. The linearity indicates that the telomere is diffusing normally relative to the surrounding chromatin.

COMPUTER SCIENCE / MATHEMATICS / PHYSICS

COMPUTER SCIENCE :: KOPPEL LAB

Caleb Leibowitz (Cooper Union, Electrical Engineering) & Joshua Lockerman (Yeshiva College & Yale, Computer Science) "Machine learning methods for text categorization"

We aim to implement several algorithms previously developed by Professor Koppel that solve several related text categorization problems. Among these problems are classifying documents by author when there is a small closed set of candidate authors, the more difficult problem of a large open set of candidate authors (the author may not be in the set of candidate authors), and the problem of authorship verification. These algorithms are so powerful that they have been somewhat successfully applied to other text categorization problems, such as deciding whether a given sentence is metaphorical or literal. This latter problem is very difficult, as the problem is not well defined.

ROBOTICS & ARTIFICIAL INTELLIGENCE :: KAMINKA LAB

Aryeh Stiefel (Yeshiva College, Computer Science) "Wrapping Player with ROS for the WBR914"

The White Box Robotics 914 PC-Bot is, essentially, a computer on wheels. The robot comes compatible with the robotic interface Player, a pseudo-operating system for many robots. Player contains several standard interfaces that enable users to interact with and control different robots, including the WBR914.

The goal of my research was to wrap the Player interface with ROS, Robot Operating System. Player contains a simpler interface than ROS, although its capabilities are not as sophisticated. Moreover, Player is extremely rigid, as it is dependent on each robot's configuration file. As a result, we wanted to write code that would take Player data and convert it into ROS topics and convert ROS commands into Player commands to control the robot, thereby enabling us to control any robot with ROS, even the robots compatible with Player.

In order to wrap Player with ROS for the WBR914, we used two Player interfaces. The first interface is the Position2d interface, which collects the PC-Bot's location and speed. Using C++ we took the Position2d information and wrote it into a ROS message, specifically geometry_msgs::Odometry. Using the Odometry ROS message type we were able to publish all the information garnered from Position2d to a ROS topic, /odom, as well as subscribe to another ROS topic that gives us another Odometry message. Using that message we were able to set the Player information needed to turn the robot in a particular direction and move it at the speed we require.

We then wrote similar code for the IR sensors, located on the WBR914. We used Player's IR interface to provide us with the range for each of the five sensors on the robot. We wanted to publish to a ROS topic, /ir_ranges, using sensor_msgs::Range but due to limitations we are unable to publish multiple ranges in a single message. Instead we chose to put each of the range data into an array of floating points and publish std_msgs::Float32MultiArray to the ROS topic. As a result we are able to choose which IR sensor we want to read, while still using ROS.

Our next step is to program the robots, using ROS, to traverse a room without bumping into anything. We are doing this by having our program read the ROS topic /ir_ranges to check each sensor to determine if there is space in any of the following directions: straight, forty-five degrees to the left and right, and ninety degrees to the left and right. Then, of the directions with space, the algorithm will pick a direction at random. The robot will turn if necessary and travel in that direction for a random distance or until it detects an object in front of it. In both cases, the robot will stop and pick a new direction.

The ultimate goal of this project is to twofold. Firstly, we want to provide our information to the public so they can easily wrap Player with ROS and enjoy ROS's complexities. Secondly, we want to program the robot to traverse hallways in order to carry packages from one location to the next, without bumping into people to maximize employee productivity.

ENGINEERING

From left to right: Naomi Schwartz, Meir Moshe Kurtz, Yael Spiegel, David Kornbluth, Daniela Garzon, Eitan Westrich, Marissa Golden

ELECTRO-OPTIC ENGINEERING :: ZALEVSKY LAB

Daniela Garzon (Stern College, Physical Sciences) "Electromagnetic scattering and absorption as related to nanoparticle dimensionality"

The optical properties of metallic nanoparticles have been studied widely and have practical use in various fields, such as medical diagnostics and therapeutics, biological imaging, and nanophotonics. The fundamental property of interest to us is the ability of the surface plasmon, the excitable electrons on the surface of the nanoparticle, to be excited by and oscillating electric field of light in order to cause absorption and scattering. Optical absorption and scattering have dominant effects at different size regions, which can be used in certain applications. The change in the strong surface plasmon absorption maximum has been used in sensor applications, while the scattering is useful in imaging methods to detect attached biosystems. For example, when coated with an antibody, nanoparticles can adhere themselves to antigens present only at the surface of cancer cells, then when electromagnetic waves are shot at the nanoparticles the scattering creates an image and can be used as a sensitive diagnostic method. For sensor and other diagnostic applications, absorption is the desired method. Therefore, it is very important to understand how the optical absorption and scattering depend on the particle's geometry and the material selection, and to find a way to control their relative contribution for the selected application. From the viewpoint of optical scattering, metal nanoparticles have attracted additional attention due to their higher tenability of resonance frequency. Thus the ability to tune the resonance wavelength of the nanoparticles as well as its ability to enhance the scattering or absorption, depending on the application, becomes extremely important in this field of nanotechnology.

Our goal was to find the dimension of a gold nanoparticle in which we can control the scattering and the absorption. Meaning, to find a nanoparticle that at different wavelengths had different peaks for scattering and absorption in order that we can control whether to scatter or absorb with the same nanoparticle depending on the wavelength of the electromagnetic light. This was done through a series of simulations using DDSCAT, a discrete dipole approximation program developed based on Maxwell's equations for the optical response of metal nanoparticles to an electromagnetic field in the visible range. DDSCAT computes the optical scattering and absorption of particles with an arbitrary geometry. Thus, by varying the dimensions of a nanoparticle, one was attained that could switch the order between the scattering and the absorption resonance and to have the scattering resonance for lower wavelengths than the absorption one. Scattering depends mostly on having a particle of greater volume, while absorption happens all of the time. We tried to create a caged nanoparticle for which the material content per volume is lower. This narrows and even reverses the gap between the scattering and absorption peaks. We found several patterns that we used to modify the dimension of the nanoparticle to obtain the results that we wanted. As the cage edge width is increased the scattering peak increases and gets closer to the absorption. Also, as all other dimensions are held constant if the width of the inner rectangle is increased the scattering peak gets closer and closer to the absorption peak. Finally we found that by increasing the width of the nanoparticle we were able to obtain a dimension where the scattering crossed over the absorption and had a higher peak (graph 1). This gives us the capability of altering

the incident wavelength to attain a higher absorption or scattering peak. This is useful for medical purposes, such as the example above. The dimensions of the successful nanoparticle as seen in fig. 1 are length = 36nm, width of the cage = 100 nm, width of the inner rectangle= 7nm, and edge width (towards the inside)= 22nm.

Our next step was to try to find a nanoparticle that could produce equally strong but separate peaks. We were able to obtain such a graph, (graph 2), by making the inner rectangle in the cage shorter than the cage. Fig. 2 is representative of such a structure. This enables us to use the particle for scattering or absorption independently. The goal now is to be able to separate the peaks more so that it is easier to control the separate wavelengths for scattering and absorption.

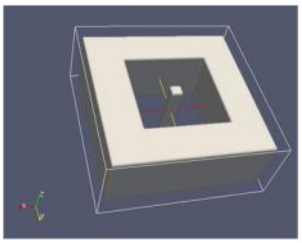

Fig. 1

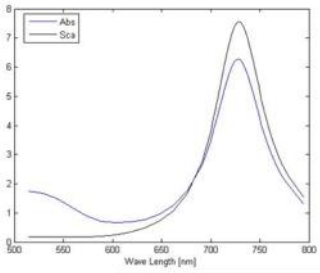

Graph 1

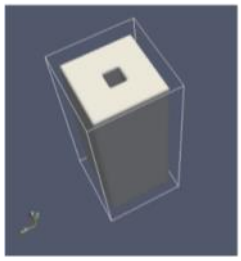

Fig. 2

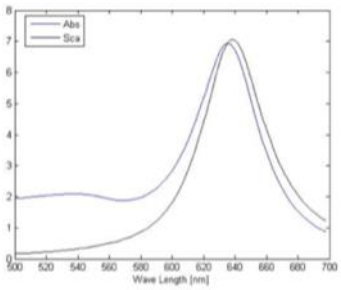

Graph 2

[1] B. T. Draine and P. J. Flatau, "Discrete-dipole approximation for scattering calculations," *Journal of the Optical Society of America A* **11**(4), 1491 (1994) [doi:10.1364/JOSAA.11.001491].

[2] K.S. Lee and M.A. El-Sayed, "Dependence of the enhanced Optical Scattereing Efficiency Relative to That of Absorption for Gold Metal Nanorods on Aspect Ratio, Size, End-Cap Shape, and Medium Refractive Index," *Journal of the American Chemical Society* August 29, 2005

COMPUTER ENGINEERING :: KEREN LAB

Marissa Golden (Stern College, Physical Sciences) "Codes for Secure Asynchronous Communication"

There are multiple ways of attacking a system in order to extract information from the system. One such attack, the Differential Power Analysis attack, measures how much power is consumed while a system makes computations and is able to determine the encryption key. GALS (globally asynchronous locally synchronous) systems are used to protect against such attacks by creating flat power consumption, and can cause a delay in a message being sent. When a binary message suffers from a random delay, the 1's can randomly be shifted one space to the left or right in a word, thus changing one word into an adjacent word. Two words are considered adjacent if one word can be mapped to the other by shifting the 1's one space to the left or right, and therefore only words of the same length and number of 1's can possibly be adjacent. For instance, set of codewords C of length n=3, from the set $F_2^3 = \{000,001,010,011,100,101,110,111\}$ the words {000} and {111} are not adjacent to any other words, whereas both {100} and {001} are adjacent with {010}, and {110}, {011}, and {101} are all adjacent with each other. A maximum of five codewords can be chosen from the set F_2^3 that can be sent securely with zero error capacity. By choosing codewords in which the zeros come in pairs or in which there is no one after a set of zeros (this will be called an "even codeword"), it is assured that none of the codewords are adjacent. For n=3, C_3={000}, {001}, {100}, {110},{111}.

In order to maximize the number of secure codewords, $|C|$, the number of groups of adjacent words must be maximized. Words can only be grouped together if all the words in the group are adjacent to each other. Once all the words are grouped, an even codeword may be picked from each group. To calculate the number of even codewords given n and the number of ones, k, if n-k is odd n'=n-k-1, otherwise n'=n-k. $m = \frac{n'}{2}$ is the number of pairs of zeros. n''=n'-m is the number of bits after squeezing pairs of zeros into one bit. The number of even codewords is $G_k = \binom{n''}{m}$. $|C| = \sum_{k=0}^{n} G_k$. The upper bound of the rate of the code is $\frac{log_2(|C|)}{n}$. Dr. Keren and Dr. Engelberg calculated the lower bound of the rate to be to be 0.6942[1] as n->∞. When I started the project Dr. Keren was able to calculate a maximum $|C|$ up to n=4, and after writing an algorithm for finding the maximum $|C|$ in MATLAB, it is now possible to calculate a maximum $|C|$ for up to n=7. A problem arose while trying to calculate the maximum $|C|$ for n=8 and k=3, as there was a group of words that did not contain an even codeword. As a result, the code rate for n=7 comes closest to the approximated lower bound.

We are currently working on either proving that it is impossible to choose more than G_k codewords, thereby proving that the calculated lower bound is tight, or finding another way of grouping and choosing codewords in order to increase the number of codewords beyond G_k.

Table 1: Code Rate for *n*=(2,3…7)

n	|C|	Upper Bound $\frac{log_2(\|C\|)}{n}$	Lower Bound $\frac{log_2(\|C\|)}{n+1}$
2	3	0.7925	0.5283
3	5	0.77398	0.5805
4	8	0.75000	0.6000
5	13	0.74009	0.6167
6	21	0.73205	0.6275
7	34	0.72678	0.6359

[1]O. Keren, S. Engelberg, "Channels with Random Delays" (In preparation)

IMAGING, MICROSCOPY AND NANOTECHNOLOGY:: POPOVTZER LAB

David Kornbluth (Yeshiva College, Physics) "Picture perfect imaging with gold and magnetic nanoparticles."

Recently, nanotechnology has attracted a lot of attention in that it provides a variety of potential applications in various fields, such as medical imaging and drug delivery. I participated in multiple projects exploring the use of nanotechnology, specifically regarding applications to medical imaging as well as the manipulation of magnetic nanoparticles within an alternating magnetic field.

Due to their unique physical, chemical and biological properties, metal nanoparticles are very attractive candidates for computed tomography (CT) contrast agents. Metallic nanoparticles have relatively high atomic numbers causing them to absorb a greater amount of radiation which will allow for a lower radiation dose to the patient. In addition, their size can be precisely controlled and they have a greater blood circulation time. Studies have shown the potential benefits of using gold nanoparticles (GNPs) as contrast agents for CT because of its unique optical properties and biosafety. We are trying to better understand the mechanism with which particles enter cells, thereby enabling us to design nanoparticles with tailored functionalities. Our hypothesis was that 2-Amino-2-deoxy-glucose (Glu-2) would be the most appropriate version of glucosamine that would penetrate cancer cells. In an attempt to find the most effective linker that would attach glucosamine to the nanoparticles, we synthesized GNPs that were 20-30 nm in diameter (see Fig. 1) and coated them with a type of polyethylene glycol (PEG), specifically PEG-7. We conducted a number of in vitro experiments to test which glucosamine (Glu-1, Glu-2, Glu-3 or Glu-6) had the highest percentage of penetration into the cells.

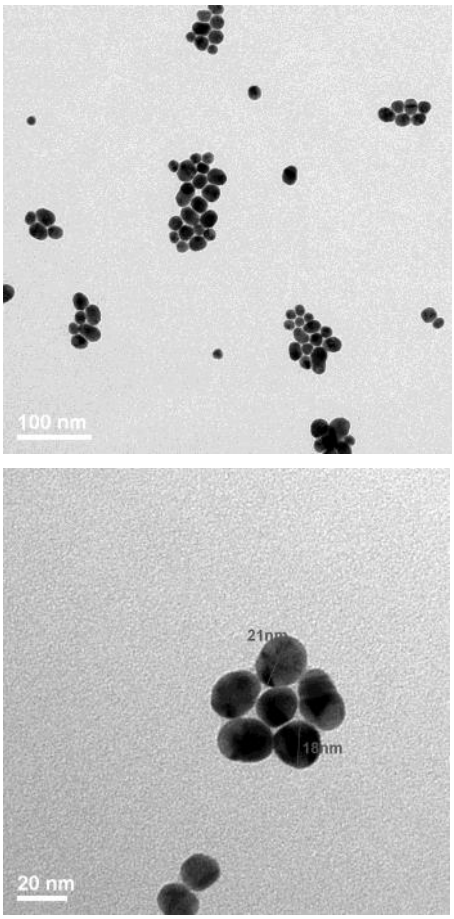

Fig. 1: Transmission Electron Microscopy (TEM) images of 20 nm gold nano-spheres

Magnetic nanoparticles, such as oxides of iron (Fe) like magnetite (Fe_3O_4) and maghemite (Fe_2O_3), are also being studied for their potential imaging capabilities. This project is based on the idea that, when subjected to an external magnetic field, the magnetic nanoparticles will vibrate differently according to their

applied coating. To begin analyzing the motion of metallic nanoparticles subject to a magnetic field we had to construct a setup to properly study such motion. To accomplish such a task we utilized the speckle phenomenon, a pattern produced from the interference of many waves of the same frequency. When illuminated by a laser, magnetic nanoparticles reflect a specific pattern (see Fig. 2) which can be analyzed to show the changes that occur due to the magnetic field. This research provides the basis for developing imaging techniques due to magnetic nanoparticle vibration within the body.

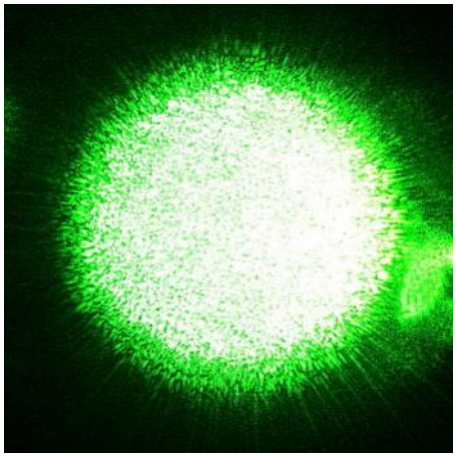

Fig. 2: Speckle pattern from a green laser as captured by a digital camera

COMPUTER ENGINEERING :: KEREN LAB

Meir Moshe Kurtz (The City College of New York, Electrical Engineering) "Secure Coding for Finite State Machines with Weighted States"

Today's electronics are becoming ever more complex and security sensitive. A modern IC chip can hold personal files, embedded software, and proprietary designs inherent to the chip's finite state machine. While the chip may be invulnerable to external data attacks, it can be vulnerable to hardware attacks.

A finite state machine uses a function of its current state and its inputs to calculate the outputs and next state, which is stored in memory. In the worst case scenario, an attacker utilizing fault injection attacks knows all the binary codewords assigned to the states, has access to the inputs and outputs, and can induce faults (flip bits) at any place in the hardware. His goal is to extract information about the device by watching how the outputs react to bit flips in the state or data. These insertions can be modeled as additive errors in a binary finite field. To prevent successful attacks, the machine's code must be created so that a checker can verify that each codeword output by the machine is a real word and has not been changed by an attacker.

For a uniform code *C*, in which at any moment the probability of being in any state is equal, the error masking probability, or the probability of an error e not being detected, is defined as $Q(e) = \frac{|\{c|c+e\epsilon C\}}{|C|}$. For an optimal uniform code $max\, Q(e) \geq \frac{2}{|C|}$. For example, for the code *C* = {1000, 0100, 0011, 1010, 0010, 0111}, $Q(1011) = \frac{|\{1000,\ 0011\}|}{6} = \frac{2}{6} = \frac{1}{3}$ since 1000 + 0011 = 1011, 0011 + 1000 = 1011, and |*C*| = 6. This can be realized if $\binom{|C|}{2} \leq 2^k - 1$, where *k* is the number of bits in the codewords. When all 2^k words are in the code, however, $\forall e\ Q(e) = 1$. To solve this problem, redundancy bits must be added to each codeword. To keep processing and memory cost low, the code must be systematic, or have redundancy bits added to the end of each word without the original bits in the 2^k words being changed. Rather they have extra bits added onto the end. Using the Punctured Cubic Code[1], $C = \{(w_k, w_r) | w_k \epsilon GF(2^k), w_r = P(w_k)^3\}$ where w_k is the information word, w_r is the redundancy word, and *P* is a permutation matrix, we can achieve $max\, Q(e) = 2^{-r+1}$, where *n* = *k* + *r*.

For weighted codes, the problem increases in complexity. For these cases, the error masking probability is defined as $Q(e) = \sum p(c)\delta(c + e\epsilon C)$ where $p(c)$ is the probability of being in state *c*. $\delta(x)$ is equal to 1 if *x* is true and zero otherwise. The problem is no longer how to equalize the number of codewords each error word hides, rather how to distribute the weights in order to lower $\max Q(e)$ for every error word while keeping $\frac{k}{n}$, the rate of the code, high. The procedure I have been following is to take an optimal uniform solution and then flip redundancy bits to increase $Q(e)$ for some error words and lower it for others. The proper weights can then be assigned to the codewords to achieve the lowest $\max Q(e)$. Using this method, I hope to find a bound on the number of flips that can be performed and the corresponding $\max Q(e)$.

---

[1]Yaara Neumeier, Osnat Keren, "Punctured Karpovsky-Taubin binary robust error detecting codes for cryptographic devices," *iolts,* pp.156-161, 2012 IEEE 18th International On-Line Testing Symposium (IOLTS), 2012

BIO-ENGINEERING :: WEISS LAB

Naomi Schwartz (Stern College, Molecular and Cellular Biology) "Challenges in quantitative fluorescence microscopy: analysis of DAPI labeled cells"

Fluorescence microscopy is used to enable visualization of cellular components such as DNA and proteins, and can be used to measure the amount of cellular components of interest. However, fluorescence depends on many environmental factors, and is therefore very difficult to quantify reliably. The goal of this project was to study the reproducibility of 4'-6-Diamidino-2-phenylindole (DAPI) labeling of DNA in cells. As DAPI is commonly used as a counterstain in fluorescence microscopy[1], its use as a fluorescence standard would be very helpful in quantitative analysis of immunofluorescence and Fluorescence In-Situ Hybridization.

B16 melanoma cells were grown on 1.5mm glass coverslips, and were fixed with either methanol or PFA, permeabilized with 0.5% Triton X100 in PBS, stained with 1.4 uM DAPI solution, and were then mounted with either Eukitt quick-hardening mounting medium (Fluka 03989), Fluoromount-G (SouthernBiotech, Birmingham, AL), or Prolong Gold (Invitrogen-Molecular Probes, Eugene, OR). For some slides, 1 micron fluorescent beads (Phosphorex, Hopkinton, MA) were added prior to mounting. The coverslips were mounted onto standard 25mm x 75mm glass slides. Five to seven fields were acquired per slide.

The slides were imaged on a Nikon TE2000E motorized inverted microscope, with a 40x/NA=1.3 oil objective. Filters appropriate to the fluorophore being imaged were selected (for DAPI, λ_{ex}=360nm , and the emission was viewed following a 400nm low pass filter). The images were acquired with a QImaging Retiga 2000 CCD camera. Images were acquired at exposure times which did not produce saturation, and dark images (i.e., with no excitation light) were acquired as well. The entire system was controlled with NIS Elements software. Images were analyzed with the Fiji distribution of ImageJ.[2,3]

Figure 1a shows a typical image of DAPI stained cells. An ImageJ macro program for automatic background estimation generated a cubic spline image which was used as the background estimate (Figure 1b), and the corrected image, with dark noise subtracted and normalized to the background autofluorescence, is shown in Figure 1c. The nuclei in Figure 1c were automatically segmented using the Spatial Fuzzy C-Means cluster analysis plugin[4] and the Huang automated thresholder in ImageJ. Beneath each image is a line-intensity profile which demonstrates the transition from the raw image to the corrected image.

The ImageJ particle analyzer was used to measure the mean intensity of the nuclei visible in each field. Table 1 shows the mean intensity of nuclei found in five different fields of one slide (prepared with a PFA fixative and a Fluoromount mounting), as well as the standard deviation and the spread of the intensities.

Table 2 shows the results of a comparison of the cell nuclei found in three PFA fixed slides, mounted with the three different mounting media.

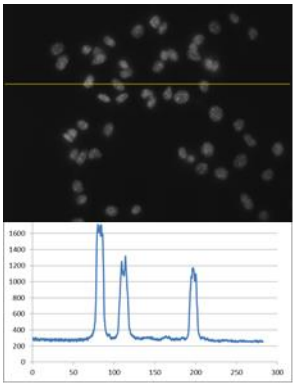

Figure 1a: Raw image of DAPI stained cells

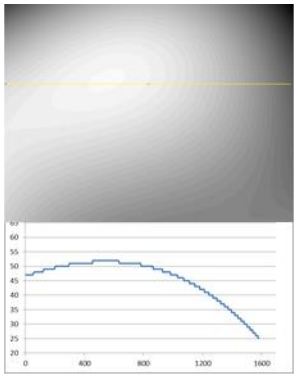

Figure 1b: Background image of DAPI stained cells

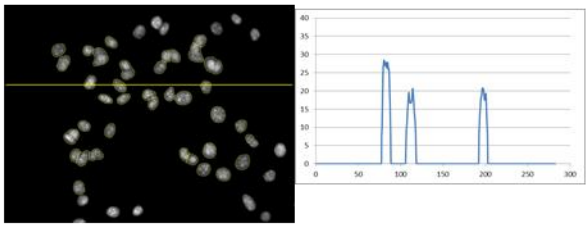

Figure 1c: Corrected image of DAPI stained cells

Field	Intensity	Std Dev	Min	Max	Max/ Min
1	23.43	3.12	17.35	29.91	1.72
2	43.1	4.5	36.73	50.34	1.37
3	12.65	2.92	7.35	19.3	2.62
4	9.35	1.88	5.63	14.27	2.53
5	14.19	2.12	10.01	18.65	1.86

Table 1: Average intensity (normalized to background) of the nuclei of DAPI stained cells found within the same coverslip fixed with PFA and mounted with Fluoromount medium.

Mounting Medium	Intensity	Std Dev	Max	Min	Max/Min
Flouromount	13.72	4.57	25.19	5.9	4.27
Prolong	14.36	4.43	25.87	6.79	3.81
Eukitt	41.64	13.09	71.42	18.82	3.79

Table 2: Average intensity (normalized to background) of the nuclei of DAPI stained cells found in separate coverslips prepared with three separate mounting media – Fluoromount , Prolong Gold, and Eukitt.

The results in Table 1 show that even within a single slide, there is a large variation in the mean intensity of the nuclei. The expected spread is 2x, which is dependent on the stage of the cell cycle. In the analysis of our slides, there are three main sources of error: dark noise estimation, background estimation, and segmentation of the nuclei. We found that the background estimation algorithm produced significantly different backgrounds even in fields within a single slide. This leads us to conclude that the background estimate is the weak link in our analysis. This problem occurs because after subtraction of the dark noise, the remaining background is very low. Therefore, the noise in the samples producing the cubic spline background estimate creates large errors when the image is normalized to the estimated background. As a result, we are now modifying the analysis to use a background image measured separately on a uniformly fluorescent slide, in order to create a more reproducible image.

[1] Life Technologies. http://probes.invitrogen.com/media/pis/mp01306.pdf. (last accessed 9 October 2011).

[2] C. A. Schneider, W. S. Rasband, and K. W. Eliceiri, "NIH Image to ImageJ: 25 years of image analysis," Nature Methods 9, pp. 671-675, July 2012.

[3] J. Schindelin, I. Arganda-Carreras, and E. Frise, "Fiji: an open-source platform for biologicalimage analysis," Nature Methods 9, pp. 676-682, July 2012.

[4] SFCM (Spatial Fuzzy C-Means. https://github.com/arranger1044/SFCM. (last accessed 4 August 2013).

BIO-ENGINEERING :: SHEFI LAB

Yael Spiegel (York University, Biomedical Science) "Neurite Growth Manipulation Through the Use of the Netrin Protein"

The goal of Dr. Orit Shefi's lab is to have a better understanding of how neurons acquire their morphology and to use the revealed mechanisms to manipulate neuronal growth. This is done with the use of Hirudo medicinalis – the medicinal leech. The leech has 21 ganglion and a head and tail, each with approximately 400 cells. These compose the central nervous system, the main topic of study in the lab.

The lab uses many techniques in order to better understand the leech including topographic and electrical cues and molecular biology. The work I did was molecular biology manipulation using the netrin protein. Netrin is an axon guidance cue that serves as a chemoattractant or chemorepellent depending on the cell receptor. The central dogma in molecular biology states that DNA is transcribed into RNA, which is then translated into a protein. Netrin has already been studied in the lab on the level of RNA. The work I did this summer with netrin was on the protein level.

In order to produce the netrin protein the RNA first had to be produced from the leech. Once this was done the RNA was converted into cDNA with the use of a reverse transcription polymerase. The netrin gene was amplified from the cDNA using specific primers and PCR. After 35 PCR cycles about 68 billion copies of the netrin gene were obtained.

After the gene was amplified and there was a large supply of the netrin gene, the netrin was cut using restriction enzymes. In addition a plasmid was cut using the same restriction enzymes. This enabled the netrin to be inserted into the plasmid using a ligase enzyme. A transformation was done in E. coli bacteria on an LB plate. Six colonies were chosen from the plate in order to complete the mini prep kit procedure. In order to verify that at least one of the six colonies contained the plasmid with the netrin the plasmid was cut and run on a gel. Two sets of results were obtained. In the first result one band was seen on the gel at 4 Kbs representing a plasmid with no insert inside. In the second result two bands were seen on the gel, one at 4 Kbs representing our plasmid and the other at 1.8 Kbs representing netrin. The latter result proved that the netrin was properly inserted, and the plasmid could then be used for a second transformation into E. coli bacteria. This transformation produced many copies of the netrin protein. The bacteria were lysed and the protein was obtained using a talon column. A Western blot will be done in order to verify that the protein produced was in fact netrin. Producing netrin will be used in order to understand the mechanism of action of the protein in nerve cells of the leech and to

manipulate the growth of neurites.

ELECTRICAL ENGINEERING :: ZALEVSKY LAB

Eitan Westrich (Yeshiva College, Pre-Engineering) "Statistics of coated nanoparticles" *

Image processing can be used to uncover a great deal of information. My project was to use image processing to understand properties of gold (Au) nanoparticles coated with silver and some other metal. The images came from a Scanning Electron Microscope (SEM), which took images over time and at different super resolutions. Using image processing techniques contained in MATLAB, we found how the particles change over time. We are interested in seeing the effects that our substrates have on nanoparticles. In this process we look for cyclical patterns of the nanoparticles to see if and how they interacted with surrounding nanoparticles. We focused on finding the number of nanoparticles in different sized circles, the area of each nanoparticle, and the distances between them.

One technique we used was to create a mask that allowed us to isolate a section of the image. The mask simplified the image by turning it from grayscale to black and white as well as taking out noise (unnecessary background). In order to accurately turn the blobs of nanoparticles white and everything else black, we needed to set a proper threshold. Now, our MATLAB function could take the centroid of each nanoparticle and calculate the distances to the other nanoparticles in that section. This gave us an average distance between nanoparticles which we can compare with average distances as the nanoparticles change over time.

Another technique to reveal information on our nanoparticles was to simplify the image and have the program locate each nanoparticle blob while eliminating blobs that touch the border. This clarifies the image by taking out particles that are only partially visible. The program then gave us the number and size of each blob in our isolated area. Next, it located for us the coordinates of each particle's centroid. Using these coordinates, we can more simply calculate average distance between particles. In order to better understand the distribution of the particles, we compared them with simulations of evenly and randomly spaced dots. Additionally, using the coordinates of each particle's centroid we could utilize a function normally used for astronomy called Two Point Correlation. This yielded information such as the likelihood of having surrounding particles within a certain radius. This information helps us better understand the physical behavior of the gold nanoparticles and can be used to optimize the coating process.

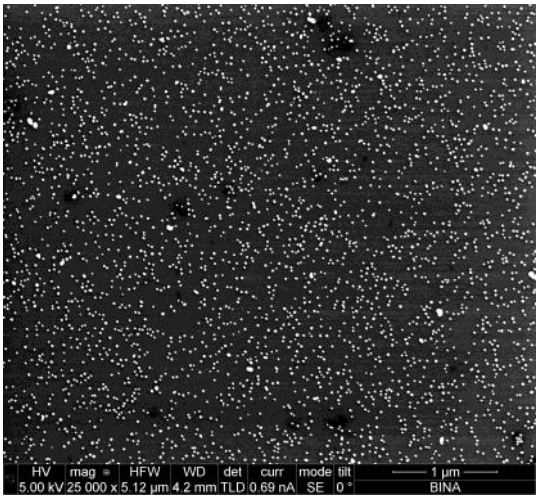

*worked with Dror Malka and Maya Aviv

From left to right: Yehuda Kupferman, Miriam Andrusier, Aaron Javitt, Avital Meiri, Uri Schneider, Allison Belfer , Nathan Farkas, Miriam Michelle Klar

MOLECULAR BIOLOGY :: COHEN LAB

Miriam Andrusier (Stern College, Biology) "The effect of SIRT6 on age-related pathologies and biomarkers of aging in male wild type and transgenic mice"

SIRT6 is a deacetylase from the mammalian sirtuin family. The upregulation of yeast SIR2 homolog was previously shown to extend lifespan in a metabolism-dependent manner. In Professor Haim Cohen's laboratory, they have managed to extend male lifespan by 15% by inserting an extra copy of the SIRT6 gene into mice. The well -known IGF-1 pathway was shown to be involved in lifespan extension. In our lab, SIRT6 is studied mainly for its role in metabolism and aging.

The main function of SIRT6 is to bind to DNA and deacetylate histones in promoter regions, thereby closing the DNA (heterochromatin structure) and inhibiting transcription. This deacetylase and DNA binding functions are found in the N-terminal region of the SIRT6 protein.

Recent results from our lab and others showed that SIRT6 is phosphorylated at both the N-terminal and C-terminal. Additionally, western blots showed that human SIRT6 runs in two bands, indicating some form of modification or alternative isoform of SIRT6. Until now, it was believed that the heavier band of SIRT6 seen in western blot was the phosphorylated protein isoform, while the lighter band was the dephosphorylated protein.

However, recent data showed that the discrepancies in molecular weight between the two SIRT6 proteins was not due to differences in phosphorylation as originally supposed, rather N-terminal cleavage. This is a modification which has not been previously associated with the SIRT6 protein. Additionally, this modification is presumed to be human specific. Mouse or bacterial expressed SIRT6 proteins run in only one band. This indicates that SIRT6 undergoes a modification that is specific to humans. This project looked to determine whether the different bands of SIRT6 are modified by N-terminal cleavage or phosphorylation.

In order to determine whether SIRT6 truly undergoes a shift in molecular weight due to phosphorylation, we exposed whole cell extract (including the SIRT6 protein) to calf intestinal phosphatase (CIP) enzyme, which removes all phosphate moieties from proteins. This ensured that SIRT6 is dephosphorylated. We then examined whether SIRT6 would run in two bands or one by electrophoresising the CIP-treated on an acrylamide gel and examining protein phosphorylation and SIRT6 levels. As seen in figure 1a, the CIP treatment indeed removed phosphorylation of all proteins examined. However, SIRT6 still ran in two bands, (fig. 1b) demonstrating that phosphorylation is not responsible for the change in SIRT6 band weight. These results show that the modification seen is not phosphorylation.

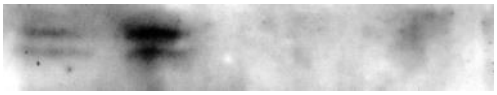

Fig 1a- P-AMPK substrate with SIRT6

Fig 1b- SIRT6 after CIP

As these preliminary results indicate a novel modification for SIRT6, we then proceeded to determine whether SIRT6 is cleaved in humans. To this end we cloned the human SIRT6 construct tagged at both ends of the protein, His-SIRT6-Flag. Fig2a depicts the cloned SIRT6 model, and Fig2b shows the successful cloned SIRT6 plasmid DNA digested with EcoRI and BAMH1 restriction enzyme and stained with ethidium bromide. After sequencing the cloned model to ensure no mutations were inserted during the cloning procedure, we continued with cell transfection.

Figure 2a- our cloned double tagged SIRT6

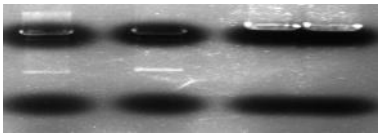

Figure 2b- double tagged SIRT6 and pcDNA vector

MOLECULAR BIOLOGY :: COHEN LAB

Allison Belfer* (Stern College, Biology) "The effect of SIRT6 on age-related pathologies and biomarkers of aging"

The increase in life expectancy of humans over the past century has raised concerns about the rise of age-related metabolic risk factors including abdominal obesity, hypertension, insulin resistance, glucose intolerance, and chronic inflammation. Much like humans, as mice age, they develop similar metabolic and immune-related disorders that can be used to model the human condition. SIRT6, a gene found in the sirtuin family, has been implicated in the extension of lifespan of male mice, and may act as a repressor of these age-related disorders. However, the mechanism by which SIRT6 extends lifespan remains largely unknown. Further research is required to determine the link between SIRT6 and aging.

To understand the effects of aging, we have chosen to study chronic inflammation, a condition occurring in older populations. This disorder, known as the "foe" side of the immune system, is caused by an imbalance of the immune system in which the body's inflammatory response no longer works to maintain the sensitiveness of the body's inflammation process, but instead begins to completely shut down the organism by inducing apoptosis of normal body cells. In order to test the efficacy of SIRT6 in mice, the spleen of both wild type and transgenic (TG) mice overexpressing SIRT6 (also called MOSES, Mouse Overexpressing Exogenous SIRT6) was assayed for signs of chronic inflammation. With a high expression of SIRT6, old TG mice at age two, showed fewer signs of this condition while old wild type mice proved to be affected by this disorder.

Cyclin-dependent kinase inhibitor 2A (p16) is a well-defined biomarker in senescence where expression in cells increases with age. Previous studies have shown that SIRT6 binds to the promoter of p16 and inhibits its expression within the cells. In turn, although the manifestation of p16 in wild type mice should increase with age, the abundance of SIRT6 in TG mice should inhibit the expression of p16, eliminating the downstream physical and genetic effects of this gene. Spleen tissue from both old and young wild type and TG mice was harvested and analyzed for p16 as a proxy for effectiveness of SIRT6 within each mouse. We show that gene expression of p16 in both young wild type and TG mice resembled that of old TG mice while old wild type mice expressed large amounts of p16.

Due to SIRT6's effect on lifespan and aging, we must not only be concerned with the presence of this gene in cells however, must also pay attention to the quantity of gene present as aging occurs. Here, we show that through reduction of chronic inflammatory episodes, SIRT6 plays a critical role in the extension of lifespan in male mice and therefore, holds tremendous promise for future interventions in metabolic disorders in humans. In order to further our understanding of this gene, research must be conducted to test if the time-specific activation of SIRT6 is enough to ameliorate effects of inflammation not only in the spleen, but in other organs and organ systems as well. The use of this knowledge will be helpful in treating an older population that may be plagued with these difficulties in the years to come.

*Asael Roichman, Haim Cohen

COMPUTATIONAL IMMUNOLOGY :: MEHR LAB

Nathan Farkas (Queens College, Neuroscience & English) "Tracking the health of your immune system: Aging and CDR3 sequence diversity"

The Mehr group's computational immunology lab is concerned with analysis of and mathematically modeling various elements of the immune system. White blood cell development, diversification, and clonal dynamics are current areas of focus.

White blood cell diversity is measured using CDR3 sequences. DNA is rearranged through a genetic shuffling process to create

many different sequences or clones. These sequences underlie the mechanics of antigen recognition and bonding, each different sequence capable of recognizing a different antigen.

Using experimental and sequenced data on CDR3 length, I worked towards identifying statistical functions of these lengths that would describe the health of an individual's immune system. I compared data from blood, spleen, lymph node, and bone marrow from both old and young patients. We hope to develop an analysis that can be performed on low cost CDR3 spectratypes that can be used to determine the health of a patient's immune system, informing decisions that depend on the immune system's health.

VIROLOGY :: GOLDSTEIN LAB

Aaron Javitt (Princeton University, Molecular Biology) "The mechanism of Varicella-Zoster-Virus entry and subsequent host cell response."

The course of varicella-zoster-virus infection (VZV) is difficult to study due to the specific requirements of the host system. Homo sapiens are the only host organism that can sustain a productive VZV infection which can present as a number of diseases including chicken pox and shingles. While a human fetal Dorsal Root Ganglion -SCID mouse model has been used with some success to demonstrate VZV infection in neurons, the cost and technical challenges of the system have not been overcome. Differentiation of H9 hESC (human embryonic stem cells) into neurons has previously been shown to be an effective host system for the study of VZV infection and the use of H9 derived neurons has yielded insights into VZV axonal transport. Given the difficulty in finding a suitable host for VZV infection, little is known about the VZV mechanisms of entry and replication. Using hESC derived neurons and human foreskin fibroblasts (HFF) as a model for infection with ORF23-GFP VZV and then subsequent analysis of mRNA expression levels through microarray analysis yielded information about the changes in neuron and fibroblast gene expression.

Based on this previously collected preliminary data, a series of experiments was designed to confirm the nature of the morphological changes occurring in infected cells. Microarray analysis alone is not a statistically significant piece of evidence alone and therefore real time polymerase chain reaction (rtPCR) analysis was needed for corroboration. HFF and hESC cell lines were infected with ORF23-GFP VZV and cDNA was extracted and analyzed through real time PCR (figure 1). Notable among the gene

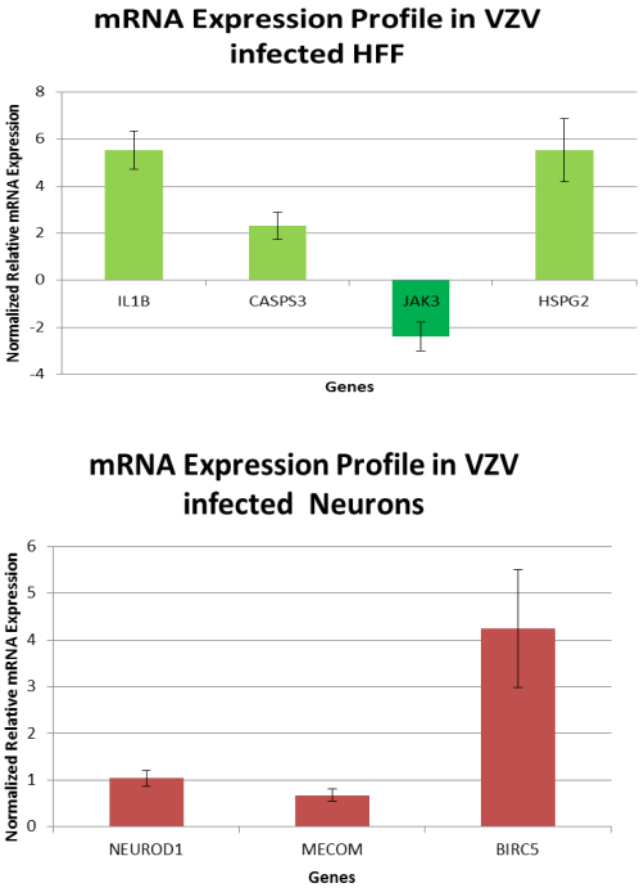

Figure 1. mrNA profile of VZV infected cells. rtPCR analysis of VZV infected HFF (top) showed a 550 percent increase in IL1-β and HSPG2, a 220%increase in CASP3 and a %230 decrease in JAK3 mRNA levels. rtPCR analysis of VZV infected neurons (bottom) showed a 100 percent increase in NEUROD1 levels, a 60% increase in MECOM levels and a 4.2% increase in BIRCS.

expression changes was baculoviral inhibitor of apoptosis repeat-containing 5 (BIRC5 or Survivin) which is upregulated in neurons during VZV infection and has been shown be an inhibitor of cell apoptosis. This supports the theory that VZV infection in neurons has an anti-apoptotic effect for a short time after the start of infection. Similarly, in HFF cells, an up-regulation of Interleukin-1 beta (IL-1β) and Caspase 3 (Casp3) demonstrate the inflammatory response and apoptotic effects of VZV infection in HFF. Janus kinase 3 (JAK3), a gene responsible for interferon signaling and cellular defense was downregulated suggesting that VZV inhibits cellular defense mechanisms during infection.

Much like the changes in cell morphology have yet to be fully classified in the course of VZV infection there has yet be a VZV receptor identified. While HFF and H9 derived neurons have been

shown to support productive VZV infections, hESC cells themselves cannot be infected by VZV. This is either due to a lack of the necessary virus replication mechanisms in the hESC or because there is no VZV receptor on hESC. Productive infection of HFF co-cultured with H9 hESC was demonstrated using fluorescently labeled magnets bound to ORF66-GFP VZV. In addition, a lack of fluorescent magnets seen in the hESC cells suggests that the virus is unable to enter the hESC cells, signifying that the cells don't possess a VZV receptor (Figure 2).Omnibus (GEO), a sub database

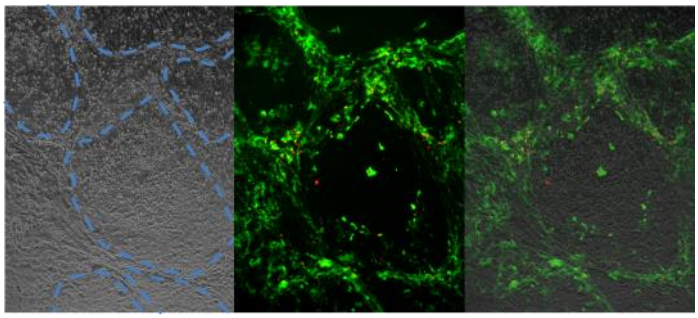

Figure 2. Phase contrast and flourescent antibody staining of co-cultured HFF and H9 hESC cells infected with VZV. (Left) 20x magnification of hESC co-cultured with HFF. The hESC colonies are outlined in blue. (Middle) 20x image of ORF66-GFP VZV infection (green) and fluoromag bound virion particles (red). (Right) an overlay of the first two images. All images were prepared with Image J and photoshop.

of base mRNA expression levels in hESC, H9 derived neurons and HFF was assembled. After the data was normalized corrected and filtered, a list of candidates for the VZV receptor was compiled. This lists includes glypican 1 (GPC1) a heparin receptor. Similar receptors have been shown to be involved in herpes simplex virus (HZV) infections which are in the same herpesvirus family as VZV. GPC1 mRNA levels were elevated in H9 derived neurons and fibroblasts as compared to hESC signifying that this may be the receptor responsible for VZV infection. In order to confirm the identity of the VZV cell membrane receptor examination of other cell types that are incapable of supporting productive VZV infections is necessary. Screening these cell types for the receptor candidates with rtPCR and immunostaining could yield new information about the membrane protein responsible for VZV entry.

VIROLOGY :: GERBER LAB

Miriam Michelle Klar[1] * (Queens College, Neuroscience and English) **"Hepatitis D protein L-HDAg interactions with host cell membrane proteins "**

Protein pathways are extremely difficult to identify and track because they are so large and numerous; viral-host cell interactions are no different. We focus on the viral-host interactions between hepatitis and cell membrane proteins. Hepatitis D is a subvirus of hepatitis B, but is unique in that it only produces one protein: the Hepatitis D Antigen (HDAg), which is expressed in large (L-HDAg) and small (S-HDAg) forms. We are now working to determine the specific protein-protein interactions involved in each protein pathway.

To do this, we use nanotechnology to perform microfluidic assays, which help us to visualize the interactions between the viral protein and the cell membrane proteins. These nanotechnology chips are made up of a control layer—a network of microchannels and valves—and a flow layer with microchannels for flowing proteins. Each chip contains either one thousand or five thousand unit cells, where each unit cell is made up of a DNA chamber for storing DNA and the corresponding protein that it produces and an interaction chamber where the protein-protein interaction occurs. Button valves are present in the interaction chambers to capture the interacting proteins. These chips are used to perform microfluidic assays, which are then scanned and the intensities of the proteins are measured.

Our initial analysis identified 233 host proteins as being a part of this protein pathway between the virus and the host cell. Of these positive interactions, we have selected those proteins involved in processes that the virus modulates, namely immune responses, cell replication, and trafficking, and retested them to confirm the initial positive interaction seen. Thus far, we have succeeded in analyzing 9 of these proteins to determine the extent of the protein expressions and the protein interactions with the L-HDAg protein.

The PTTG1IP-L-HDAg interaction shows an intensity of 1400 a.u. TSG101 (ESCRT-1 complex component, vesicular trafficking, retrovirus budding), STT3A, ATP6V0C (vacuolar ATPase, host-virus interactions), TUSC3, PERP (apoptosis, cell adhesion), and SEC63 (translocation of proteins across the endoplasmic reticulum) all showed florescence intensities between 700-1000 a.u. COA1 (mitochondrial inner membrane, translocation, nuclear assembly, COX assembly) had an intensity of about 500 a.u. TSPO has a veryow florescence intensities (<200 a.u.). Additionally, we have also determined the protein-protein affinity of L-HDAg to TSG101, ATP6V0C, STT3A, and PTTG1LP (Figure 1).

We are continuing to verify the L-HDAg-cell membrane protein interactions so that we can rank the importance of each protein interaction. At that point we will be able to research the biological meaning and effect of all these interactions by increasing and/or decreasing protein levels. A change in protein interactions will demonstrate a biological effect. We will also look at the localization of the proteins, which are mostly concentrated in the nucleus. By increasing protein levels, the overexpression of certain proteins may

change expression patterns, demonstrating an interaction.

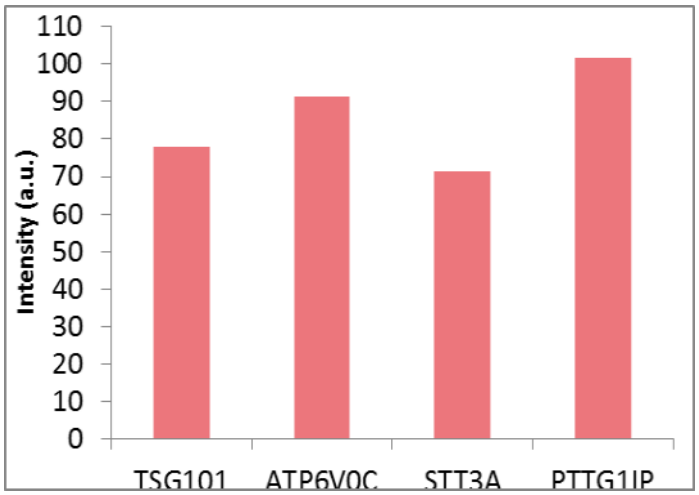

Figure 1a.

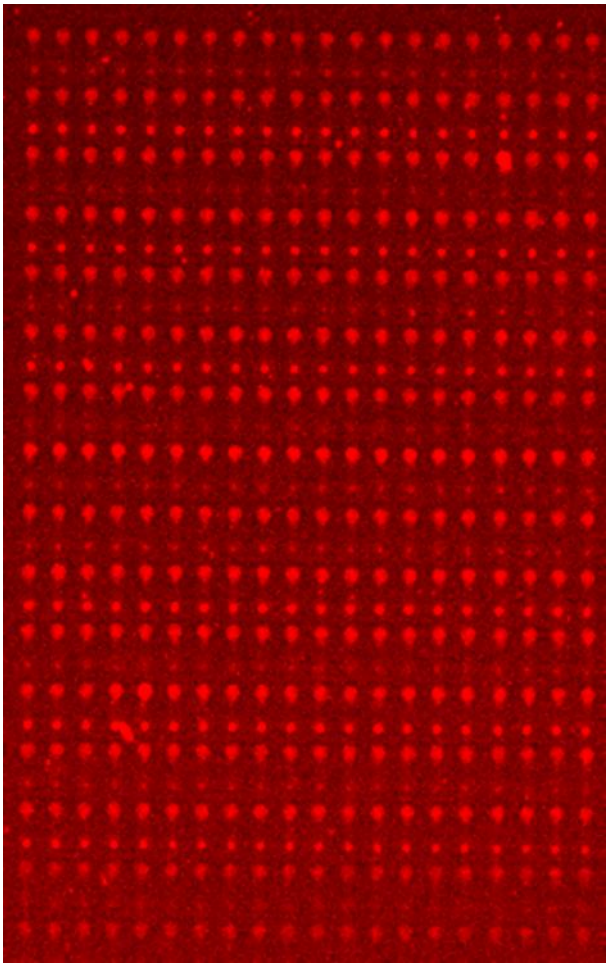

Figure 1b. The buttons capturing the interactions between the viral protein and four membrane proteins. From top, in groups of four: TSG101, ATP6V0C, STT3A, PTTG1LP.

*Ya'ara Ben-Ari[2], and Dr. Doron Gerber[2]

[1]Queens College, CUNY, Flushing, NY

[2] The Mina & Everard Goodman Faculty of Life Sciences, The Nanotechnology Institute, Bar-Ilan University, Ramat Gan, Israel

MOLECULAR PARASITOLOGY :: MICHAELI LAB

Yehuda Kupferman (Queens College, History) & Uri Schneider (Yeshiva College, Biology) "Exosome excretion of defective spliced leader RNA is a mechanism of isolating infected *T. brucei* and *L. major* cells"

The Michaeli lab studies post-transcriptional gene regulation in eukaryotic parasites. *Trypanosoma brucei* and *Leishmania major* are two species of such parasites that are utilized as models for research, as they are easily genetically manipulated organisms and fairly controllable.

T. brucei and L. major are usually transmitted into a mammalian host via the tsetse or sand fly, respectively, where they then undergo morphological and antigenic variation. The parasites infect the midgut of the fly host and then migrate to the salivary glands. This movement enables the parasites to be transferred to a mammalian host. Additionally, T. brucei and L. major are the causative agents for parasitic diseases such as leishmaniosis, African sleeping sickness, and Chagas' disease. These parasites attack the mammalian immune system and cannot be killed once transmitted into a mammal host. The only known methods of care include: treatment of the symptoms or stopping the parasite in its tracks before transmission. Our lab focuses on the method of RNA silencing as a means to prevent the T. brucei and L. major from infecting the mammalian host.

RNA silencing is a natural eukaryotic process that serves to regulate protein synthesis and protein functioning. Genes in messenger RNA are suppressed by small non-coding RNAs called "small nuclear RNAs" (snRNA) that form an RNA-protein complex called "small nuclear ribonucleoproteins" (snRNP). The mRNA is silenced via a process called RNA interference (RNAi), which blocks and breaks down the mRNA without it ever leaving the cell's nucleus. Other small nucleolar RNA (snoRNA) edit and modify mRNA so that certain genes are expressed and others are silenced.

Our research utilizes RNA silencing with a focus on looking for innovative and effective ways of treating the diseases caused by *T. brucei and L. major. Trypanosoma brucei and Leishmania major* have an exosomal excretion process in which they use to communicate with other infected cells in the mammalian host by a

process called trans-splicing. This process is controlled by an SL RNA (spliced leader RNA) and allows the spliced leader to donate a common exon to other mRNAs. Silencing part of the SL RNA or other mutations during biogenesis of the spliced leader lead to the export of defective SL RNA via the endosomal sorting complex required for transport (ESCRT)[ii]. These processes change the spliced leader into a complex called SL-RNP-C. This, in turn, serves as a quorum sensing mechanism that disables the exosome excreting cell from joining in social motility with other infected cells.

Interestingly, cancer cells have a similar exosomal excretion process in which they excrete micro RNAs into their microenvironment in order to affect gene expression of neighboring cells. As these parasites and cancer cells have similar exosomal excretion mechanisms, finding a way to isolate infected cells and mutate the biogenesis of spliced leader RNA in parasites can lead to safer and more effective chemotherapy treatments.

Experiments were done under the supervision of Dror Eliaz and Michael Jerafi of Professor Shulamit Michaeli's lab.

Eliaz, Dror *et al. "Exosome excretion containing defective spliced leader RNA is a novel quorum sensing mechanism in trypanosomes." Diss. (unpublished). Bar-Ilan University, 2012. Print.*

Eliaz, Dror. "Spliced leader RNA discard (SLD) – a novel pathway to excrete RNA from trypanosomes." Diss. (unpublished). Bar-Ilan University, 2013. Print.

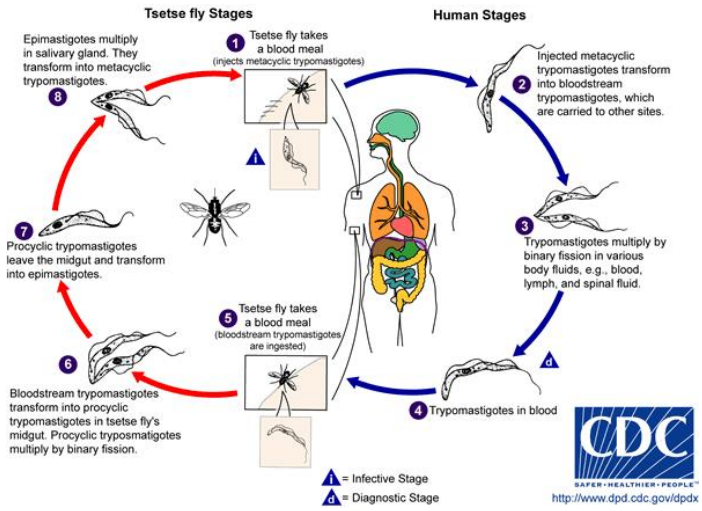

[i]

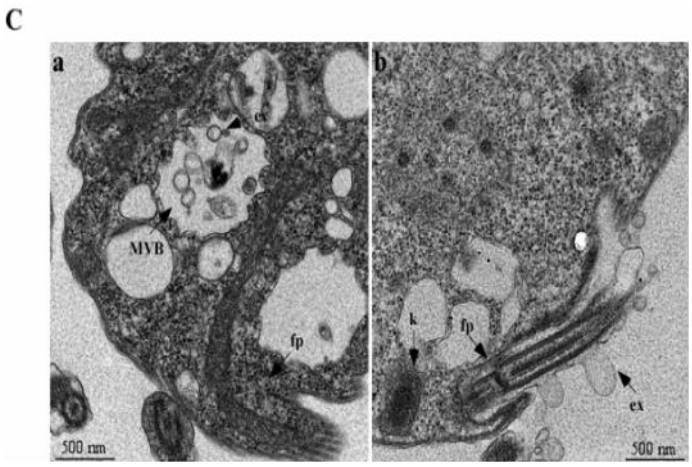

[ii] Picture on the left contains the MVB's that have ESCRT. On the right, exosomes are being excreted from the parasite via the flagellar pocket.

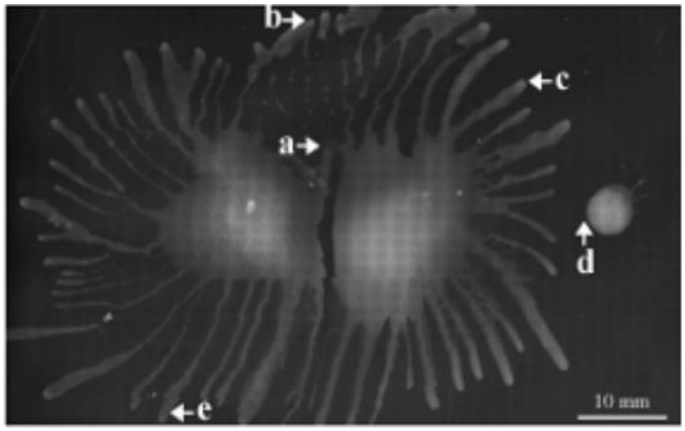

[iii]The two healthy Trypanosoma parasites to the left are joining together in social motility while disassociating from the sick cell on the right.

MOLECULAR BIOLOGY :: GINSBERG LAB

Avital Meiri (Stern College, Biology) "SK1 gene silencing and its biological effects on E2F1"

E2F1 is a nine-polypeptide transcription factor from the E2F family. It binds to a specific gene promoter sequence and enhances expression of those genes. E2F1 is involved in many cellular processes including cell cycle progression, DNA replication, DNA damage and repair checkpoints, and apoptosis. It is an oncogene and is therefore strictly regulated. It is mainly down regulated through binding to the tumor suppressor retinoblastoma (pRB). When the cells receive a signal to proliferate, pRB is

hyperphosphorylated, undergoes a conformational change and releases E2F1 allowing it to activate the transcription process. This regulation occurs in wild type cells with a normal phenotype. However, in many tumors, pRB is inactivated and E2F1 activity is therefore unregulated.

E2F1 affects the expression of Sphingosine Kinase 1 (*SPHK1). The SPHK1 gene encodes for SPHK1 protein which phosphorylates sphingosine, a sphingolipid, and produces sphingosine-1-phosphate (S1P). S1P is a molecule that can act as a second messenger and take part in cell signaling. It may signal the cell to induce cell proliferation and inhibit apoptosis as well as stimulate other responses thus contributing to tumor progression.*

A series of experiments were designed to study the regulation of E2F1 on SK1 and determine the effects of SK1on the biological activity of E2F1. To investigate this, SK1. U2OS, a human osteosarcoma cell line, with exogenous E2F1 (ER-E2F1) was used. Transfection was done using two small interfering RNAs (siRNAs) and a nonspecific (control) RNA. SK1 silencing was investigated by means of protein analysis and RNA quantification. The project focused on the apoptotic activity of E2F1. Methods used to examine apoptosis included cleaved Caspase 3 immunostaining and Fluorescence Activated Cell Sorting (FACS) using Annexin Propidium Iodide (PI) and PI alone. Results demonstrated a greater amount of SK1 protein in U2OS samples with a longer activation of E2F1. In addition, more apoptotic cells were observed in samples where SK1 was silenced compared to samples treated with non-specific control RNA. The data concludes that SK1 acts to inhibit apoptosis caused by E2F1.

NEUROSCIENCE / PSYCHOLOGY

From left to right: Ruth Ruben, Elisheva Laks, Kayla Gasner, Shaina Sedighim, Josh Siegel

NEURODEVELOPMENTAL PSYCHOLOGY :: GEVA LAB

Kayla Gasner (York University, Kinesiology) "The effect of music on affect in adults"

On a superficial level, listening to music seems like a passive process. However, studying music in the fields of psychology and physiology, it is clear that music plays an active role both on a conscious and subconscious level. Music has the ability to alter affect in both a stimulatory and relaxation manner. Heart-rate, blood pressure and dermal temperature are typical methods of measuring affect changes in humans and have been traditionally used in earlier research. The research on causal effects of music on affect is inconclusive; although there are logical explanations and predictions, this particular field has not been developed fully. There is great opportunity to ask questions and explore this field in greater detail.

Some research has shown that rap music correlates to increased stimulatory effects, which presents itself with angry and aggravated behavior and distrust in peers (Ballard and Cotes, 1995). In a more positive application, relaxation and self-regulation occurs best when preferred calming music is played, rather than any other type of calming music (Theorell and Lingham, 2009). Affective reaction to music is highly dependent on one's perception (Scherer and Zenter, 2001) and personal style (Theorell and Lingham, 2009).

It has been suggested that there is an innate ability in humans to expect and predict musical sequence. In the absence of practical musical training and from a young age, humans are able to detect flaws in rhythm and harmonic structure. The detection in a minute manipulation of musical structure by an infant supports the hypothesis of innate ability to predict and expect musical structure. Preliminary research on music and affect has been conducted on infants, but the data has no yet been successfully analyzed.

The aim of this experiment is to monitor the sensitivity of musical structure patterns, expressed by behavioral changes when listening to segmented fragments of songs in adults. Using video recordings and an eye tracker device (Tobbi), various behavioural psychological were coded.

The instructions given to the subjects (n=30) was to sit quietly, look at the screen and listen to the music. Eight tracks of music were played- four composed by Beethoven and four composed by the Beatles. The sequencing of the tracks were in particular orders: normal, backwards, repetitive or jumbled. No instruction or explanation of the type of music was given to the subject. After the experiment, each subject filled out a demographic survey and a questionnaire regarding their experience.

Coding of data was recorded every ≤5 seconds, on a categorical parametric scale. Six categories with 2-6 sub-parameters were measured at each time interval. With confidence in inter-rater reliability ($k=0.965$, $p<0.001$), the data was analyzed using SPSS.

We found that the duration of state was particularly sensitive to changes in structure in classical music rather than in pop music ($t=4.215$, $df=29$, $p=0.001$). This means that the change in structure of the Beatle's composition did not affect the state to the same degree as the Beethoven composition. As well, it was found that musicians (classified as subjects with ≥ 4 years of musical training) were more calm during structural changes than non-musicians

(F=4.594, df=28, p=0.41).

Theoretical explanations for these findings must be researched further. Future research should include an analysis of the remaining data collected from the adults and a deep investigation into the connection between the adult and infant data collected.

PSYCHOLOGY :: GILBOA-SCHECHTMAN LAB

Elisheva Laks (Queens College, Psychology and Education) "SAD voices"

Social anxiety disorder (SAD), otherwise known as social phobia, is a mental disorder where an individual has marked anxiety about social or performance situations, in which there is a fear of embarrassing oneself under scrutiny by others (DSM-IV, APA 2000). Socially anxious individuals have been reported to have problems in their social relations (e.g., Gilboa-Schechtman et al., in press).One facet impaired in SAD is non-verbal communication, some of them related to conveying dominance or submission in social situations. Ratings of dominance were inversely related with individuals who have SAD in vocal and eye-gaze performance (Mallott et al., 2009). These nonverbal features have been shown to play an important role in conveying emotions (Laukka and Elfenbein 2011) and in conducting power negotiation (Scherer 1986; Scherer et al., 2003).

Acoustic analysis has the potential to offer a subtle understanding of the ways in which individuals negotiate interpersonal interactions. Yet, acoustic analysis has, until recently, been under-utilized. We believe it offers a way to understand corrective actions people take following exclusion. Acoustic analysis of speech is emerging as a noninvasive and sensitive measure of emotional state (Juslin and Laukka 2004; Elfenbein and Ambady 2002) which can lend insight in detecting anxiety in a person's tone of voice. Dominance is associated with low levels of F0, vocal intensity, and speaking rate. In addition to acoustic indicators of dominance, research has shown to differentiate between vocal profiles of different intents; command utterances have increased MF0 and intensity compared to neutral statements (Galili et al., 2013).

Our most recent study examined the changes in feelings of belongingness amongst individuals with social anxiety. Subjective and expressive measures were analyzed in response to exclusion, acceptance, and popularity amongst high and low socially anxious individuals. 'Cyberball,' a virtual ball toss game, served as the manipulation between the different states of emotional inclusiveness.

Results indicate that exclusion among low socially anxious individuals promotes increased vocal confidence (as indicated by decreased mF0 and increased vocal intensity in uttering commands), whereas high socially anxious individuals delineated decreased vocal confidence. Following popularity, women (but not men) with high social anxiety exhibited a decrease in mood and self-esteem. Seeking to understand the reactivity to changes in belongingness enhances clinical research and scholastically paves the road to understanding the core mechanisms of SAD.

OCULAR MOTILITY & VISUAL PERCEPTION :: ZIVOTOFSKY LAB

Ruthie Ruben (CUNY Brooklyn College, Psychology and Biology) "Gauging the effectiveness of the 'Red-Green Duochrome' test"

The "Red-Green Duochrome" test is used by optometrists as verification that a proposed correction is accurate for their patient. The test is performed during refraction and uses a half green-half red chart with black numbers on it. If the proposed correction has the right power, the patient will see both the red and green side equally sharp. The test utilizes the phenomenon of chromatic aberration to examine the focal points of parallel rays of green and red light entering the eye with respect to the retina.

Some previous literature suggests that The Red-Green test be performed prior to determining the cylindrical component of the prescription, as others disagree and state it be performed after determining the cylindrical component of the prescription. However, because sphero-cylindrical eyes with only a spherical correction still have a component of myopic defocus on the retina, the assumption that the duochrome test is reliable given the two sets of rays on the retinal plane is questionable. As such, this experiment was carried out to compare the interval of patient responses during the duochrome test with and without a cylindrical correction.

Autorefractometry and autokeratometry were performed and recorded. The interpupillary distance was then measured manually using a millimeter ruler. Subsequently, all subjects were examined with a full subjective examination under the supervision of a certified Israeli optometrist to determine the full refractive prescription. The red-green test was performed monocularly with a phoropter in a dark room under conditions of spherical correction only and additionally with sphero-cylindrical correction. For subjects with cylindrical corrections lower than or equal to 0.50 Diopters, a cylindrical correction of +0.50 X 180 degrees and -0.50 X 90 degrees was induced using a Jackson Cross Cylinder (JCC). The order of eyes tested (right or left) and the condition (spherical or

sphero-cylindrical) were randomly determined. All subjects were fogged by the addition of a +1.00 Diopters to the prescription placed in the phoropter. Subjects were then instructed to concentrate on the black numbers on the green half of the chart and briefly compare them to the black numbers on the red half of the chart. They were then asked to report which background provided a clearer or sharper image. The prescriptions yielding the last "red" response, the first "green" response and the "equal" response were recorded.

The range between the last "red" response and the first "green" response was calculated for each eye and each experimental condition (spherical correction only and spherico-cylindrical correction) and compared using a paired, two-tailed t-test. The data were analyzed both as a group and separately for the induced cylindrical correction and physiological cylindrical correction sub-groups.

Twenty- three Bar-Ilan staff and students (12 males, 11 females) between the ages of 20 to 56 (mean age: 24.3 ± 7.5) participated in the experiment. Spectacle wearers were preferred because the goal of the study was to determine if the duochrome test interval of responses differed with differing refractive corrections. As such, the refractive error composition of the recruited subjects was higher than would be expected from the population norms. Thirty two eyes required a spherical refractive correction or a spherico-cylindrical refraction with a cylindrical component less than 0.75 Diopters. In these eyes, the spherico-cylindrical condition was induced. Twelve eyes contained a physiological astigmatism larger than -0.75 Diopters.

The mean refraction of all eyes in the study for the spherical component was -3.00 Diopters and for the cylindrical component was -0.65 Diopters. The mean spherical equivalent refraction in the study was -3.35 Diopters. Twenty nine eyes had a compound myopic astigmatism, eight were simple myopes, one was a simple myopic astigmat, three were emmetropic (refractive correction between zero and a quarter of a Diopter), and none were simple or compound hyperopes.

One subject was not included in the analysis because she was not able to determine a refraction for which she reported that the "green" was clearer. For the rest of the subjects, each of the 41 eyes was treated individually when comparing the interval between "red" and "green" responses obtained in the spherical correction only and spherical-cylindrical correction conditions. These intervals were not significantly different (p=0.2). The intervals for the subgroup with induced astigmatism and physiological astigmatism with and without cylindrical correction were also not significantly different (p=0.45 and p=0.25, respectively).

The interval of "red" to "green" responses did not differ significantly between the conditions in which the cylinder was corrected and in which it was not corrected. Therefore, it can be concluded that the red-green duochrome test can be used both before the JCC and after the JCC test in the subjective refraction. The research was approved by the Helsinki committee at Bar Ilan University (Ramat-Gan, Israel), and subjects signed a statement of informed consent prior to their participation in the study. Subjects from the student body and staff at the university volunteered to participate in the study and did not receive remuneration for their participation.

MOLECULAR NEUROSCIENCE :: APPELBAUM LAB

Shaina Sedighim (University of California, Los Angeles, Neuroscience) "Gephyrin: molecular manager of inhibitory synapses ."

Gephyrin is a multifunctional protein that has been established to both be responsible for molybdenum cofactor synthesis and involved in membrane protein-cytoskeleton interactions. This project concerns Gephyrin's latter function and hopes to demonstrate the protein's role as an inhibitory synaptic cluster protein.

The Appelbaum lab concerns itself with the categorization and elucidation of molecular and cellular mechanisms that underline various sleep disorders and psychomotor retardation through the zebrafish model. The confirmation of Gephyrin's association with inhibitory receptors (as a cluster protein) in specific zebrafish neurons (that were previously shown to be involved with the sleep cycle) would provide a strong reference point for future projects that look to investigate synaptic connections involving such receptors.

Through cross-breeding and immunofluorecsent screening experiments, this project looked to confirm the effectiveness of certain genetic constructs that express GPHN by attempting to visualize the physical association of Gephyrin with inhibitory synaptic markers in the hypothalamus and spinal cord through confocal microscopy.

A transgenic line of zebrafish in which Gephyrin is fused to the hcrt promotor and enhanced Green Fluorescent Protein (hcrt:GPHN-eGFP) was produced. Hcrt, or Hypocretin (Orexin) Neuropeptide Precursor, is a gene that codes for two mature neuropeptides (hypocretin/orexin A and hypocretin/orexin B) by proteolytic processing. These neuropeptides, which bind to orphan G-protein coupled receptors HCRT1 and HCRT2, have been proven to function in the management of sleep and arousal.

Hcrt:GPHN-eGFP adult zebrafish brain sections showed GFP expression within the hypothalamus in the expected temporal and

spatial pattern upon immunofluorescence analysis (Fig. 1).

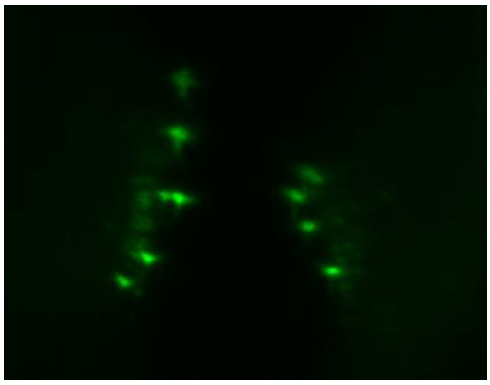

Co-immunofluourescence studies with anti-Glu4 (red) and anti eGFP (green) succeeded to show that GPHN does not co-localize with such excitatory synapses (Fig. 2). Similar findings were made with anti-Glu2

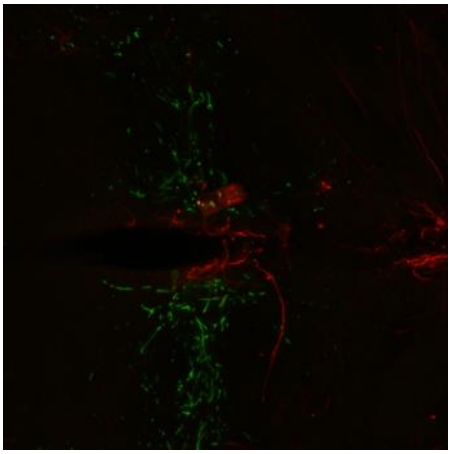

studies. However, co-immunofluourescence of anti-GlyR (red) and anti-eGFP (green) in adult zebrafish slices failed to demonstrate the expected co-localization result. This finding demonstrates that the hcrt:GPHN-eGFP line is not a sufficient model to study the clustering patterns of GPHN. Larval co-immunofluourescence studies with Hcrt: GPHN-eGFP progeny (6dpf) showed nearly identical results to above mentioned adult zebrafish brain analyses.

A similar immunofluourescent blot was carried out in which hcrt:GPHN-eGFP x 1013 line 6dpf progeny larvae were (individually) immuno-stained with anti-eGFP/anti-Gly, anti-eGFP/anti-Glu2, and anti-eGFP/anti-Glu4. Spatial neuronal expression of the 1013 line was not previously confirmed; thus, the speculation that GPHN would co-localize with Glycine in the spinal cord was proven to be false, as anti-eGPF (green) showed expression of GPHN in the notochord. Glu2 and Glu4 patterns were as expected. Therefore, 1013 is an inadequate model to show GPHN expression.

In order to better confirm GPHN's inhibitory synaptic presence, Narp:Gal4 x uas:GPHN-eGFP larvae will be studied. Identical immuno-staining antibodies will be utilized along with anti-GABA. Attempts to confirm co-localization of GPHN and GlyR in narp:gal4-uas:dsRED (+/-) x uas:GPHN-eGFP did show a co-localization signal (Fig.3).

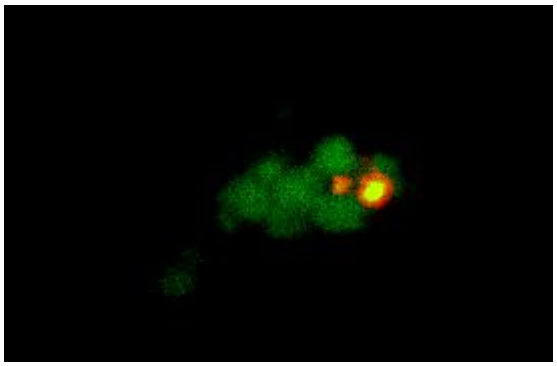

However, this could be regarded as a false-positive, as there was no guarantee that the selected larval candidates were dsRED (-/-). This, utilizing a parental line that is certainly dsRED (-/-), and demonstrating co-localization of GPHN and GlyR, would conclusively prove that GPHN is indeed a post-synaptic inhibitory protein.

OCULAR MOTILITY AND VISUAL PERCEPTION :: ZIVOTOFSKY LAB

Josh Siegel (Yeshiva University, Philosophy and Biology) "Ocular motion and improved mechanisms of testing predictive saccades ."

Through the study of ocular motion, much can be learned about perception and the brain. While the relationship isn't readily apparent, many areas of the brain manifest themselves through different types of eye movements. The specific types of eye movements that I am studying are known collectively as saccadic eye movements. A saccadic eye movement occurs when your eye makes a rapid motion in order to focus specific objects within your field of vision onto the fovea of the eye, resulting in optimal resolution.

There are essentially two types of saccadic eye movements, reactive saccades and predictive saccades. Reactive saccades occur when the eye tracks the movement of an object to a random location at a random time. These eye movements generally show a latency of approximately 200ms with respect to the movement of the target. However, it has been shown that a periodically oscillating target elicits a different type of eye movement, predictive saccades. When the eye makes predictive saccadic movements, the latency observed is generally <80ms and can approach zero.

In a recent study performed by Joiner and Shelhamer, they deduced from the relationship between reactive and predictive saccades that the brain has a built in 'internal clock mechanism' that

allows for the ability to make predictive saccades. While subjects were observing a moving target within the predictive range, the frequency of the moving object was lowered to the reactive threshold. When this occurred, the subjects' eyes made multiple saccadic movements before adjusting to the lower frequency.

The salient question that must be addressed, is, what is the evolutionary purpose of the predictive saccade mechanism? It has been shown that such a mechanism exists, and it has been concluded that the mechanism is enabled when the movement of an object alternating between two fixed locations exceeds ~0.5 Hz. The first step in answering the above question is to acquire as much information about predictive saccades as possible. Once the nature of the mechanism is fully understood, we can then begin to understand its utility and apply this knowledge further.

The goal of my research project is to alter the generic test for predictive saccades and observe how the predictive mechanism is affected. Generally predictive saccades are observed when a target moves back and forth between two locations at a constant frequency. I created three different tests in order to see how the predictive mechanism would function under different conditions:

The first test created is what we called rectangular waves, because of the graph that was produced. Instead of the target remaining in each of the two locations for an equal amount of time, the target remained at one location between 200ms-400ms longer than it remained in the other location. As can be seen in the graph, the brain managed to eliminate any latency even when two temporal qualities needed to be considered. This test was performed at varying frequencies.

The second test had the subject follow a target that moved between three locations, as opposed to the previously tested two locations. This test was performed at three frequencies.

The third test had the subject follow a target that moved between five locations. This test was performed at three frequencies.

The data for the various tests is still being collected and analyzed with the hope to gain further insight into the nature and purpose of predictive saccades.

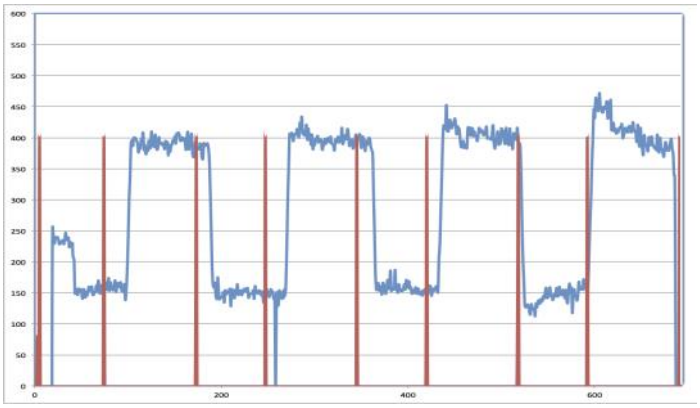

1. Shelhamer, Mark, and Wilsaan M. Joiner. "Saccades exhibit abrupt transition between reactive and predictive, predictive saccade sequences have long-term correlations." *Journal of Neurophysiology* 90.4 (2003): 2763-2769.

2. Joiner, Wilsaan M., and Mark Shelhamer. "An internal clock generates repetitive predictive saccades." *Experimental brain research* 175.2 (2006): 305-320.

3. Y-axis=location of subject's horizontal gaze; X-axis=time; Red lines represent the movement of the target; Blue lines represent the movement of subject's gaze.